

# Flow-induced Non-Hermitian Topology in Ordinary Elastic Matter

Tsvi Tlusty\*

Center for Soft and Living Matter, Institute for Basic Science, and  
Physics and Chemistry Departments, Ulsan National Institute of Science and Technology, Ulsan 44919, Korea  
(Dated: December 23, 2024)

Open non-Hermitian systems exhibit unique topological hallmarks that are absent from their isolated Hermitian counterparts. Our model system demonstrates that these exotic topological phenomena can be induced in the spectra of generic elastic lattices, simply by subjecting them to low-Reynolds viscous flow. The interplay of hydrodynamics and elasticity splits Dirac cones into bulk Fermi arcs, pairing exceptional points with opposite half-integer topological charges. The emergent singularities organize the spectral bands in geometric patterns reflecting the underlying symmetry breaking. The present findings suggest that non-Hermitian physics can be explored in ordinary dissipative matter, living and artificial alike.

## INTRODUCTION

The conservation of energy in isolated Hermitian systems is a basic tenet of physics, but in practice, most systems are open, exchanging energy and information with the external world. This inherent non-Hermiticity is traditionally seen as an inevitable imperfection of realistic systems, yet recent studies revealed that it gives rise to distinctive phenomena unmatched in Hermitian physics [1]—most notably skewed spectral bands prone to symmetry breaking when exceptional points emerge [2–6]. This discovery kicked off intensive efforts to engineer non-Hermitian systems in diverse classical and quantum settings, ranging from photonics [7–10], phononics [11–13], and optomechanics [14] to electronics [15] and atomic lattices [16]. The potential prowess of non-Hermitian technology has been demonstrated in developing new meta-materials and devices, such as media with loss-controlled transparency [17] or directional invisibility [18], and ultra-sensitive detectors [19, 20].

But an open question remains: besides sophisticated engineered systems, can one observe and utilize these so-called exotic topological phenomena in more common and natural settings?—After all, we are immersed in a dissipative, non-Hermitian world, and living systems are immanently open to exchange with the surrounding environment at all scales. An important pioneering step into this dissipative regime are recent studies by Vitelli and coworkers who modeled and simulated the emergence of non-Hermitian “odd” elastodynamics in a network of active elements designed to exert circular forces [21, 22]. Here, we suggest that the answer to the open question above is positive: simple model and simulations show that non-Hermitian topological hallmarks can be easily obtained by tuning the interplay of conservative and dissipative forces in standard, *passive* elastic networks subject to ordinary viscous flow. Unlike the innovative designs in [21, 22], the present system requires no specific active elements, but merely laminar background flow. As

we discuss in the following, such settings are omnipresent in the overdamped low-Reynolds regime, typical to cells, macromolecules and simple soft matter systems, suggesting that non-Hermitian topology is much more common in this regime than previously realized.

Among the exotic phenomena observed in non-Hermitian materials, *bulk Fermi arcs* [7] hold a special place. In contrast to the ingrained intuition that frequency levels are closed curves, each Fermi arc is an *open* isofrequency curve ending at two exceptional points. These endpoints are defects with opposite half-integer topological charges. It is important to note that bulk Fermi arcs are topological hallmarks of non-Hermiticity in the bulk spectrum of the lattice, unlike the more familiar *surface* Fermi arcs induced by Weyl points in 3D Hermitian systems [23–26]. Bulk arcs have been so far elusive and were empirically observed in one photonic crystal [7]. Strikingly, the present work finds that the elusive bulk arcs are a *generic* phenomenon of driven viscoelastic matter whose emergence does not require fine tuning and stems directly from the symmetry of the interactions.

In the following Results section, we first derive the dynamic equations of the hydro-elastic lattice and calculate its vibrational spectrum in the momentum space. Then, we demonstrate how the interplay of Hermitian and skew-Hermitian interactions splits the Dirac cones into bulk Fermi arcs pairing exceptional points. Next, we show that the emergence of arcs is a generic hallmark of the flow-induced non-Hermitian dynamics. We discuss the topological features of these singularities and their links to the density of states. Finally, in the Discussion, we examine possible realizations of our model system, potential implications and future extensions of our study.

## RESULTS

**The motion of the hydro-elastic lattice.** To see how non-Hermitian topology arises in ordinary elastic matter at low-Reynolds, consider the following model system (Fig. 1A). A two-dimensional triangular lattice made of spherical particles of size  $\ell$ —joined by thin elastic struts

\* [tsvitlusty@gmail.com](mailto:tsvitlusty@gmail.com)

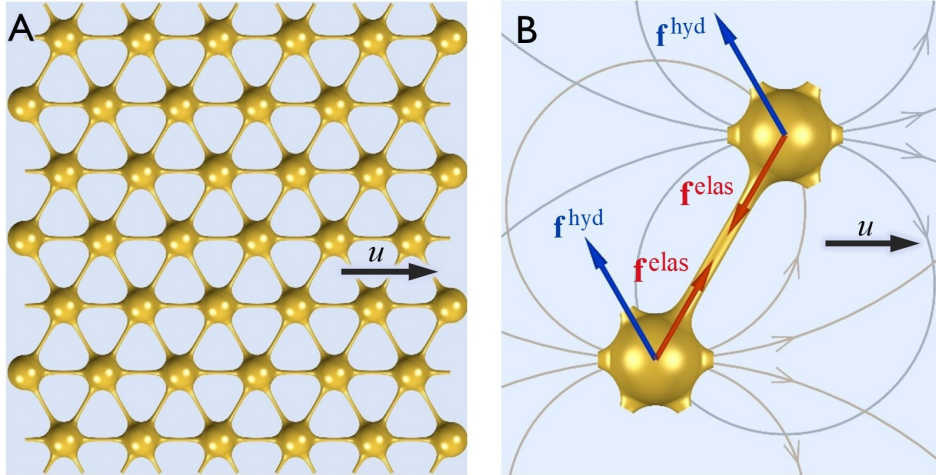


FIG. 1. (A) A triangular lattice made of spheres connected by elastic struts is immersed in a thin layer of viscous fluid between two walls in the  $z$  direction (perpendicular to the page). The lattice is driven at a velocity  $u$  relative to the fluid. (B) A pair of moving particles induce dipolar flow fields (grey streamlines), thereby exerting on each other equal hydrodynamic forces,  $\mathbf{f}_{ij}^{\text{hyd}} = \mathbf{f}_{ji}^{\text{hyd}}$  (blue arrows) in the direction of the induced flow. The elastic forces along the elastic strut are opposite,  $\mathbf{f}_{ij}^{\text{elas}} = -\mathbf{f}_{ji}^{\text{elas}}$  (red arrows), thus conserving linear momentum.

of length  $a$  and spring constant  $\kappa$ —is submerged in a viscous fluid of viscosity  $\eta$  and is moving at a velocity  $u$  relative to the fluid. The resulting viscous drag on each particle is  $\gamma u$ , where  $\gamma$  is the friction coefficient. Such relative motion can be obtained in the lab by holding the lattice in a flow or by driving the lattice with various forces (see Discussion).

Perturbing the surrounding fluid, the driven particles induce long-range interactions throughout the lattice [27–30] (Fig. 1B). When the flow is limited to a thin sheet of viscous fluid between solid floor and ceiling, these hydrodynamics forces are dipolar [31, 32], and the force exerted by particle  $j$  on particle  $i$  is

$$\mathbf{f}_{ij}^{\text{hyd}} = \gamma u \ell^2 R_{ij}^{-2} \begin{bmatrix} \cos 2\theta_{ij} \\ \sin 2\theta_{ij} \end{bmatrix}, \quad (1)$$

where  $\mathbf{R}_i$  are the particle positions and the distance vectors are  $\mathbf{R}_{ij} = \mathbf{R}_i - \mathbf{R}_j = R_{ij}(\cos \theta_{ij}, \sin \theta_{ij})$ . The magnitude of the hydrodynamic dipole in (1) scales as  $\sim u \ell^2$ . The Hookean elastic forces are proportional to the change of the length,  $\Delta R_{ij} = R_{ij} - \bar{R}_{ij}$ , where  $\bar{R}_{ij}$  the equilibrium length of the springs ( $a$  in the lattice),

$$\mathbf{f}_{ij}^{\text{elas}} = \kappa \Delta R_{ij} \begin{bmatrix} \cos \theta_{ij} \\ \sin \theta_{ij} \end{bmatrix}. \quad (2)$$

Owing to the dipolar symmetry of (1), the hydrodynamic forces a pair of particles exert on each other are equal,  $\mathbf{f}_{ij}^{\text{hyd}} = \mathbf{f}_{ji}^{\text{hyd}}$  (because  $\theta_{ji} = \pi + \theta_{ij}$ ). Thus, the dipolar forces break Newton's third law of momentum conservation (Fig. 1B). This is because viscous flow is an inherently open system, an *effective* representation of energy and momentum transfer from hydrodynamic degrees-of-freedom to microscopic ones. To steadily move the lattice, the momentum leakage ('loss') needs to be constantly compensated by the driving force ('gain'). In contrast, the elastic forces (2) are opposite and conserve linear momentum,  $\mathbf{f}_{ij}^{\text{elas}} = -\mathbf{f}_{ji}^{\text{elas}}$ . As shown below, the interplay of conservative and non-conservative forces give rise to skewed non-Hermitian topology.

Two timescales govern the dynamics of the lattice: the hydrodynamic timescale  $\tau_{\text{hyd}} = a^3/(u \ell^2)$ , and the elastic relaxation time  $\tau_{\text{elas}} = \gamma/\kappa$ . Their ratio is the hydroelastic number,

$$\epsilon \equiv \frac{\tau_{\text{elas}}^{-1}}{\tau_{\text{hyd}}^{-1}} = \frac{\kappa a^3}{\gamma u \ell^2}, \quad (3)$$

which controls the system's behavior: when  $\epsilon \ll 1$ , it is dominated by hydrodynamics, and when  $\epsilon \gg 1$  by elasticity. Hereafter, we measure times in units of the hydrodynamic timescale  $\tau_{\text{hyd}}$  and frequencies in  $\tau_{\text{hyd}}^{-1}$ .

The dynamical equations combine Stokes flow with Hookean elasticity, a linear regime where the correspondence between experiment and theory is well-established. In this overdamped regime, the friction force on each particle is counterbalanced by the driving force,  $\mathbf{F} = F \hat{x}$ , and by the hydrodynamic and elastic interactions in the lattice,

$$\gamma \dot{\mathbf{R}}_i = \mathbf{F} + \sum_{j \neq i} (\mathbf{f}_{ij}^{\text{hyd}} + \mathbf{f}_{ij}^{\text{elas}}), \quad (4)$$

where  $\dot{\mathbf{R}}_i$  is the  $i^{\text{th}}$  particle's velocity (see App. A 1). In equation (4), the long-range hydrodynamic forces (1) are summed over all particles, while elastic interactions (2) are summed only among neighbors connected by struts. Owing to the lattice parity symmetry, the sums of interactions vanish at steady-state, when the lattice traverses uniformly at a velocity  $u = F/\gamma$ .

**Dynamics in momentum space.** The coaction of elastic and hydrodynamic forces excites collective motion in the lattice. Expanding the dynamics (4) in small deviations  $\mathbf{r}_j$  of the particles from their steady-state positions in the moving lattice  $\bar{\mathbf{R}}_j$ , we find that the collective modes are plane waves  $\mathbf{r}_j = |\mathbf{k}\rangle \exp[i(\mathbf{k} \cdot \bar{\mathbf{R}}_j - \omega t)]$  (App. A 2–A 3). The 2D polarization of the wave,  $|\mathbf{k}\rangle$ , is an eigenstate of a non-unitary Schrödinger-like equation with an eigenfrequency  $\omega$ ,

$$\mathcal{H} |\mathbf{k}\rangle = \omega |\mathbf{k}\rangle, \quad (5)$$

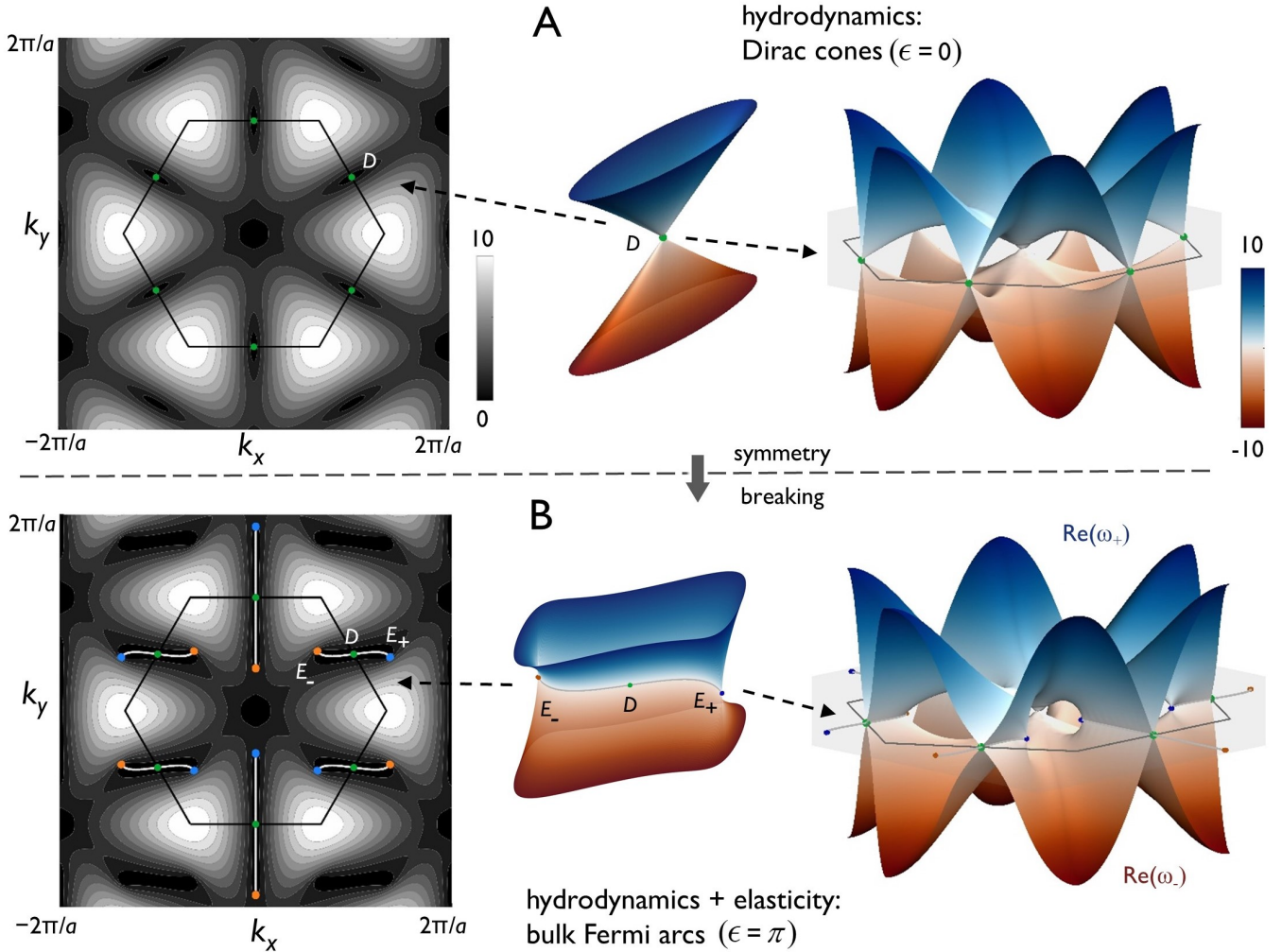


FIG. 2. (A) A purely hydrodynamic system,  $\epsilon = 0$ . Left: The operator  $\mathcal{H} = \mathcal{H}_{\text{hyd}}$  is Hermitian with real frequency bands  $\omega_+ = -\omega_- = \sqrt{\Omega_x^2 + \Omega_y^2}$ . The spectrum exhibits six Dirac points (green, one denoted as D) on the boundary of the Brillouin zone (black hexagon). Middle: At each Dirac point, the bands merge, forming a graphene-like double-cone, “diabolo” shape. Right: the 3D shape of the frequency bands in the first Brillouin zone (grey hexagon), showing the double-cones, which are halved by the zone’s boundary. (B) At  $\epsilon \neq 0$ , the symmetry is broken when  $\mathcal{H}$  includes a skew-Hermitian component,  $\epsilon \mathcal{H}_{\text{elas}}$ . Left: The real part of the bands,  $\text{Re}(\omega_+) = -\text{Re}(\omega_-)$ , drawn for  $\epsilon = \pi$ , exhibits six bulk Fermi arcs (white lines) in the first Brillouin zone (the whole spectrum is shown in Fig. 7). Each arc splits from a Dirac point (green) and joins two Exceptional Points (ExPs) with topological charges  $\pm \frac{1}{2}$  (orange and light blue,  $E_+$  and  $E_-$  are two ExPs that split from D). Middle: the real parts of the bands merge along the Fermi arc, forming a double-wedge shape. Right: 3D shape of the the frequency bands in the first Brillouin zone (grey hexagon), showing the double-wedges (halved by the zone’s boundary).

where the operator  $\mathcal{H}$  is a momentum-space representation of the forces in the lattice. The “Hamiltonian”  $\mathcal{H}$  is a  $2 \times 2$ -matrix, which sums the hydrodynamic and elastic interactions with a relative weight  $\epsilon$ . In the basis of left- and right-circular polarizations, we obtain

$$\begin{aligned} \mathcal{H} &= \mathcal{H}_{\text{hyd}} + \epsilon \mathcal{H}_{\text{elas}} , \\ \text{with } \mathcal{H}_{\text{hyd}} &= \Omega_x \boldsymbol{\sigma}_x + \Omega_y \boldsymbol{\sigma}_y , \\ \text{and } \mathcal{H}_{\text{elas}} &= -i(\omega_x \boldsymbol{\sigma}_x + \omega_y \boldsymbol{\sigma}_y + \omega_1 \mathbf{1}) , \end{aligned} \quad (6)$$

where  $\boldsymbol{\sigma}_x$ ,  $\boldsymbol{\sigma}_y$  and  $\mathbf{1}$  are Pauli’s and the unity matrices. The frequencies  $\Omega_x$ ,  $\Omega_y$ ,  $\omega_x$ ,  $\omega_y$  and  $\omega_1$ , are the Fourier

sums of the interactions—all real by the parity symmetry of the lattice (see App. A 3). The hydroelastic operator  $\mathcal{H}$  (6) is analogous to the Hamiltonian of spin- $\frac{1}{2}$  particles in a complex 2D magnetic field with damping [33], and this spinor-like nature shows in the spectrum, as discussed below.

**Symmetry: Parity and Hermiticity.** The hydrodynamic operator  $\mathcal{H}_{\text{hyd}}$  in (6) is Hermitian, a sum of products of Hermitian Pauli matrices and real numbers. Likewise, the elastic operator  $\mathcal{H}_{\text{elas}}$  is skew-Hermitian (*i.e.*, a

Hermitian operator multiplied by  $i$ ),

$$\mathcal{H}_{\text{hyd}} = \mathcal{H}_{\text{hyd}}^\dagger, \quad \mathcal{H}_{\text{elas}} = -\mathcal{H}_{\text{elas}}^\dagger.$$

Note that the hydrodynamic forces do not conserve momentum, but the effective hydrodynamic operator is Hermitian. This is because, in the low-Reynolds regime, the sum of the forces is proportional to the velocity (the drag force in (4)). Mathematically speaking, the imaginary unit factors of the time derivative ( $i\omega$ ) and the spatial derivative ( $i\mathbf{k}$ ) cancel each other. For the same reason, the effective elastic operator is skew-Hermitian, reflecting the overdamped nature of elastic modes in this regime. As for parity symmetry in  $\mathbf{k}$ -space, the hydrodynamic part is odd and the elastic part is even,

$$\mathcal{H}_{\text{hyd}}(-\mathbf{k}) = -\mathcal{H}_{\text{hyd}}(\mathbf{k}), \quad \mathcal{H}_{\text{elas}}(-\mathbf{k}) = +\mathcal{H}_{\text{elas}}(\mathbf{k}).$$

This follows from the parity of the interactions (1,2):  $\Omega_x$  and  $\Omega_y$  are odd functions of  $\mathbf{k}$  whereas  $\omega_1$ ,  $\omega_x$  and  $\omega_y$  are even (see App. A 3).

**The spectrum: Dirac cones and Fermi arcs.** The interplay of odd, Hermitian hydrodynamics and even, skew-Hermitian elasticity brings about distinctive topological signatures (Fig. 2). The spectrum of equations (5,6) exhibits two eigenfrequency bands,

$$\omega_{\pm} = -i\epsilon\omega_1 \pm \sqrt{\nu_+ \nu_-}, \quad (7)$$

where  $\nu_{\pm} = (\Omega_x - i\epsilon\omega_x) \pm i(\Omega_y - i\epsilon\omega_y)$ , and all frequencies are measured in units of  $\tau_{\text{hyd}}^{-1}$ . The corresponding polarization eigenstates are (App. A 4)

$$|\mathbf{k}_{\pm}\rangle = \frac{1}{\sqrt{|\nu_+| + |\nu_-|}} \begin{bmatrix} \sqrt{\nu_{\pm}} \\ \sqrt{\nu_{\mp}} \end{bmatrix}. \quad (8)$$

Without elastic forces (Fig. 2A), a purely hydrodynamic system ( $\epsilon = 0$ ) exhibits real spectrum of propagating phonon-like waves [27, 28],  $\omega_+ = -\omega_- = (\Omega_x^2 + \Omega_y^2)^{1/2}$ . On the edge of the Brillouin zone there are six Dirac points where the hydrodynamic interaction vanishes,  $\Omega_x = \Omega_y = 0$ . At a Dirac point, negative and positive bands kiss,  $\omega_+ = \omega_- = 0$ , forming a graphene-like double cone [34] (App. A 6).

The introduction of skew-Hermitian elasticity at non-zero  $\epsilon$  breaks the symmetry. Fig. 2B shows the real part of the bands,  $\text{Re}(\omega_+) = -\text{Re}(\omega_-)$ , for a hydroelastic number  $\epsilon = \pi$  (the whole spectrum is shown in Fig. 7). Six bulk Fermi arcs—four S-shaped and two vertical lines—emerge from the Dirac points. Along the arcs, the real parts of the bands merge at  $\text{Re}(\omega_+) = \text{Re}(\omega_-) = 0$ . Each arc is therefore an *open-ended* isofrequency contour joining a pair of *isolated* exceptional points (ExPs). As shown below, these points are topological defects of opposite  $\pm\frac{1}{2}$  charges (App. A 7).

**Singularities and bifurcations.** At the ExPs, the spectral bands (7) and their corresponding eigenstates (8)

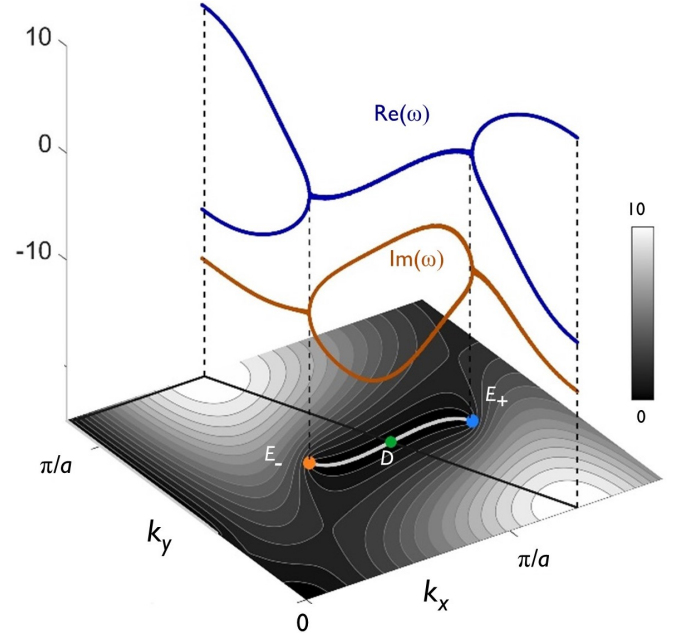


FIG. 3. The double branching transition in the real (blue) and imaginary (red) parts of the bands at the exceptional points (10). Zoom on the upper right bulk Fermi arc in Fig. 2B.

simultaneously coalesce (Fig. 2B): the bands are purely imaginary,  $\omega_+ = \omega_- = -i\epsilon\omega_1$ , and the coalescing eigenstates,  $|\mathbf{k}_+\rangle = |\mathbf{k}_-\rangle$ , are either right- or left-circular polarizations, reflecting the chirality of the topological charges (see App. A 7). ExPs occur where the determinant in (7) vanishes, (*i.e.*, when  $\nu_+ = 0$  or  $\nu_- = 0$ ) yielding the condition,

$$\frac{\Omega_y}{\omega_x} = -\frac{\Omega_x}{\omega_y} = \pm\epsilon. \quad (9)$$

At these double branching singularities, of both  $\text{Re}(\omega)$  and  $\text{Im}(\omega)$ , the spectrum becomes gapless. In contrast to the Dirac points whose eigenspaces are two-dimensional, the eigenstates at the ExPs are parallel, signifying a reduction of the eigenspace dimension to one.

Tuning the hydroelastic number  $\epsilon$  advances the ExPs along 1D trajectories, from the Dirac points at  $\epsilon = 0$  to the corners or the center of the Brillouin zone at  $\epsilon = \infty$  (App. A 7). Along these trajectories, the bands exhibit square-root singularities (Fig. 3),

$$\omega_{\pm} = -i\epsilon\omega_1 \pm \sqrt{(\omega_x^2 + \omega_y^2)(s^2 - \epsilon^2)}, \quad (10)$$

where  $s \equiv \Omega_x/\omega_y = -\Omega_x/\omega_y$  is a 1D coordinate defined by (9). The Fermi arc is the branch-cut of the square root (10) stretching between the bifurcation transitions at the ExPs,  $s = \pm\epsilon$ . The square-root singularity reflects strong level repulsion between the bands, compared to the linear opening of the gap at the Dirac cone [9].

**Bulk Fermi Arcs are generic.** As mentioned, the *bulk* Fermi arcs are topological signature of non-

Hermiticity [7] in the driven elastic lattice—unrelated to the more common *surface* Fermi arcs induced by Weyl points in 3D Hermitian systems [23–26]. The bulk arcs are a direct outcome of the broken symmetry, at  $\epsilon \neq 0$ , when hydrodynamics and elasticity with opposite symmetries are mixed. Thus, the bulk arcs are a *generic* feature of the system, which are indeed observed in other lattice symmetries (Fig. 9) and for all directions of the driving flow. This is formally shown by a small- $\epsilon$  expansion around the Dirac cone of a purely hydrodynamic system (App. A 8), demonstrating that solutions to the ExP double condition (9) always exist. Thus, the pair of ExPs and the bulk arc that stretches between them are generic.

**Topological charges.** The ExPs are topological defects: a closed eigenfrequency loop encircling an ExP cannot shrink to a point without passing through the ExP. The corresponding topological charge can be found from the vorticity of the band-gap [4],  $\Delta\omega = \omega_+ - \omega_-$  (Fig 4),

$$\mathcal{V} = -\frac{1}{2\pi} \oint \mathbf{d}\mathbf{k} \cdot \nabla_{\mathbf{k}} (\arg \Delta\omega) . \quad (11)$$

Since the band-gap is  $\Delta\omega = 2\sqrt{\nu_+ + \nu_-}$  (7), the vorticity is

$$\mathcal{V} = -\frac{1}{4\pi} \oint \mathbf{d}\mathbf{k} \cdot \nabla_{\mathbf{k}} (\arg \nu_+ + \arg \nu_-) = \pm \frac{1}{2} , \quad (12)$$

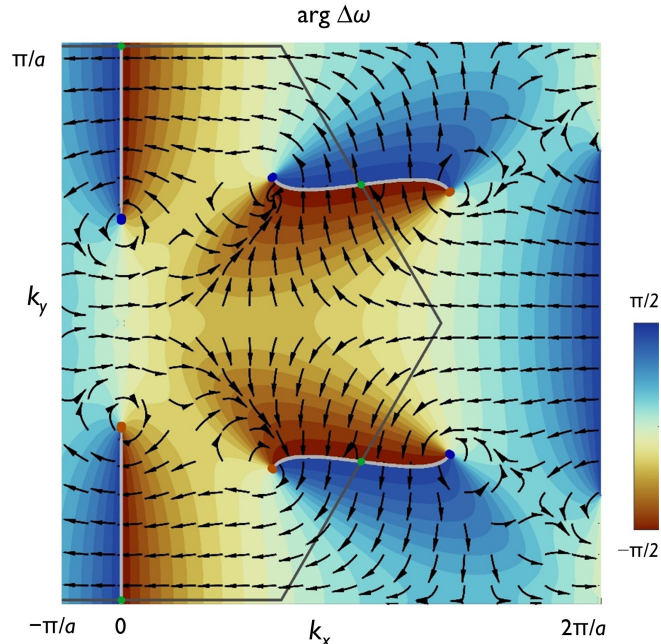


FIG. 4. The vorticity of the band-gap,  $\Delta\omega = \omega_+ - \omega_-$  (11), for  $\epsilon = \pi$ . The argument of the band-gap,  $\arg \Delta\omega$ , is color-coded and arrows denote its gradient field,  $\nabla_{\mathbf{k}}(\arg \Delta\omega)$ . Hexagonal black line shows the Brillouin zone boundary, with Dirac points (green) and exceptional points with  $\pm \frac{1}{2}$  charges (orange and blue).

with a sign corresponding to the left- or right-handed chiralities of the gradient field (App. A 10). The vorticity is determined by the branch-cuts, where the jumps of  $\arg \nu_{\pm}$  by  $\pm 2\pi$  yield the topological charges  $q_{\pm} = \pm \frac{1}{2}$ . The charges and their opposite chiralities originate from the square-root singularity of the Riemann surface (10), and reflect the spinor-like nature of the polarization eigenstates, which accumulate a  $\pm\pi$  phase when circling the ExP and passing through the branch-cut of the arcs.

Likewise, the charges can be computed from the integral of the Berry phase [35] (see App. A 9). Berry's connections are the vectors

$$\mathcal{A}_{\pm}(\mathbf{k}) = i \langle \mathbf{k}_{\pm} | \nabla_{\mathbf{k}} | \mathbf{k}_{\pm} \rangle ,$$

and Berry's phases  $\gamma_{\pm}$  are the loop integrals

$$\gamma_{\pm} = \oint \mathcal{A}_{\pm}(\mathbf{k}) \cdot d\mathbf{k} = \pm\pi . \quad (13)$$

The corresponding charges,  $q_{\pm} = \gamma_{\pm}/(2\pi) = \pm \frac{1}{2}$ , are determined by the jump of the phase (13) at the branch-cut, as in the case of the vorticity (11).

**The density of states and its singularities.** Projecting the Riemann surfaces of the spectral bands  $\omega_{\pm}$  onto the complex frequency-plane reveals the density of states  $g(\omega)$  (Fig. 5),

$$g(\omega) = \left(\frac{a}{2\pi}\right)^2 \int d^2\mathbf{k} \delta(\omega - \omega(\mathbf{k})) . \quad (14)$$

The Dirac points (green) split between the two banks of the branch cut. Notable are sharp-edged ridges of the density merging at logarithmically diverging summits, akin to van Hove singularities in Hermitian systems [36]. Level repulsion shows in low density of states around the ExP singularities in Fig. 5. The analytic density of states  $g(\omega)$  is similar to the one obtained from spectra of simulated lattices, with deviations owing to finite size and boundary conditions (Fig. 10).

## DISCUSSION

**Realizations and physical limitations.** After expounding on the topological hallmarks of the present non-Hermitian model system, we turn to discuss possible realizations. In estimating the experimentally accessible regime, four physical conditions come to mind:

I. The topology is most notable when the elastic and hydrodynamic forces are comparable, around  $\epsilon \sim 1$ . From the definition of  $\epsilon$  (3), this condition can be expressed as  $\kappa \sim \eta u(\ell/a)^3$  (using Stokes law  $\gamma \sim \eta\ell$ ).

II. The Reynolds number  $Re$  must be kept in the over-damped non-inertial regime,  $Re = \rho u \ell / \eta \leq Re_*$ , with an upper bound  $Re_* \simeq 10^{-2} - 10^{-1}$ . Using condition I, this amounts to an upper bound,  $\kappa \leq Re_* [\eta^2 / (\rho \ell)] (\ell/a)^3$ .

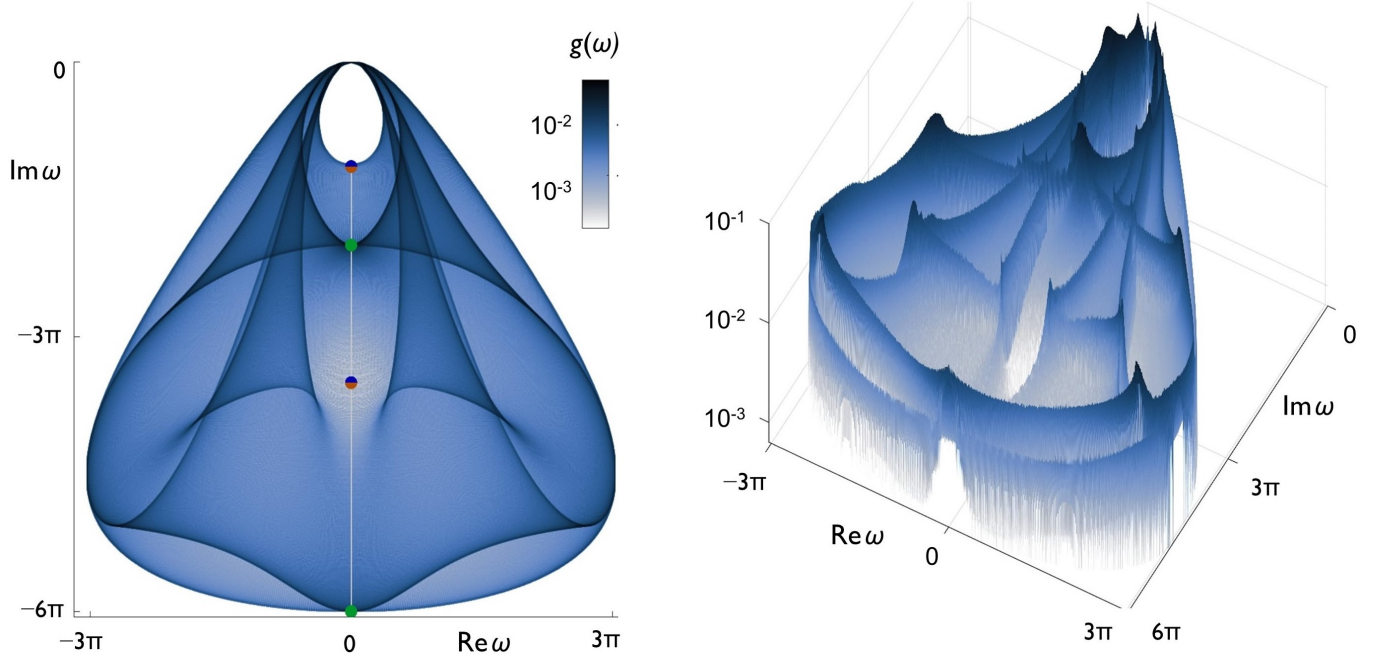


FIG. 5. Left: The density of states  $g(\omega)$  plotted in log-scale, showing the Dirac points (green circles) and the exceptional points (blue/orange circles), all connected by bulk Fermi arcs (white line) at  $\text{Re } \omega = 0$ . Right: 3D representation of  $g(\omega)$ .

III. To avoid lattice “melting” and masking of the spectrum, the thermal fluctuations should be kept small. Expressed as a Lindemann-like criterion, this implies that the fluctuations are smaller than the particle size,  $\langle \mathbf{r}_i^2 \rangle \sim (k_B T / \kappa) \ln(L/a) \leq \ell^2$ , where  $k_B T$  is the thermal energy scale and the fluctuations of the 2D elastic lattice increase logarithmically with its size  $L$  [37]. This condition is recast as a lower bound on the elasticity,  $\kappa \geq (k_B T / \ell^2) \ln(L/a)$ .

IV. The dynamics should be fast enough to allow adequate collection of statistics,  $\eta \ell / \kappa \sim \tau_{\text{elas}} \sim \tau_{\text{hyd}} \leq \tau_*$ , with an upper bound taken as  $\tau_* \sim 10 \text{ s}$  [27, 30]. This sets another lower bound on the elasticity,  $\kappa \geq \eta \ell / \tau_*$ .

Combining the four conditions I-IV brackets the elastic strength  $\kappa$  within the range:

$$\max \left[ \frac{k_B T}{\ell^2} \ln \frac{L}{a}, \frac{\eta \ell}{\tau_*} \right] \leq \kappa \sim \eta u \frac{\ell^3}{a^3} \leq \text{Re}_* \frac{\ell^3}{a^3} \frac{\eta^2}{\rho \ell}. \quad (15)$$

Examination of the bounds in the  $\ell-\kappa$  plane (Fig. 6) shows that the regime defined by (15) is easily accessible in standard soft matter settings. For example, consider a prototypical quasi-2D microfluidic system, where particles of size  $\ell \sim 10 \text{ } \mu\text{m}$  are driven at velocities  $u \sim 10^2-10^3 \text{ } \mu\text{m/s}$  in oil of viscosity  $\eta \sim 30 \text{ cP}$  [30]. Taking a geometric factor  $(\ell/a)^3 \sim 0.1$  (for  $a \sim 20 \text{ } \mu\text{m}$ ), we find from condition I that the optimal spring constant is  $\kappa \sim 10^2-10^3 \text{ kBT}/\mu\text{m}^2$ . The Reynolds number of this flow,  $\text{Re} = \rho u \ell / \eta \sim 10^{-5}-10^{-4} \ll \text{Re}_*$ , is well within the overdamped regime set by condition II. Even in a relatively large lattice of  $(L/a)^2 \sim 10^4$  particles, the lower

bound on the spring constant set by condition III is much smaller than the optimal value,  $\kappa \geq (k_B T / \ell^2) \ln(L/a) \sim 0.05 \text{ kBT}/\mu\text{m}^2$ . Finally, the statistics collection condition IV sets a tighter lower bound  $\kappa \geq \eta \ell / \tau_* \sim 10 \text{ kBT}/\mu\text{m}^2$ . Thus, we see that all conditions I-IV (15) are met by

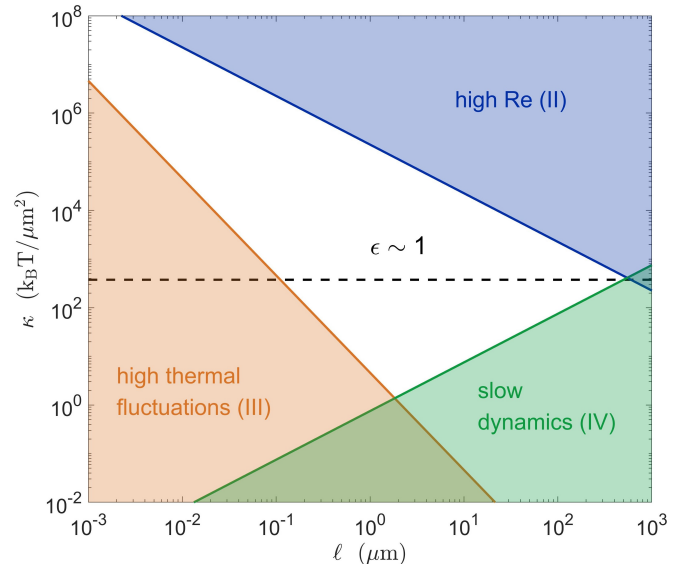


FIG. 6. The physical limitations I-IV in the  $\ell-\kappa$  plane, drawn for velocity  $u = 500 \text{ } \mu\text{m/s}$ , viscosity  $\eta = 30 \text{ cP}$ , geometric factor  $(\ell/a)^3 = 0.1$ , and lattice size  $(L/a)^2 = 10^4$ . The regions excluded by bounds II-VI are shaded, and condition I ( $\epsilon \sim 1$ ) is the dashed line. The accessible region (15) is in the remaining white domain.

the optimal spring constant  $\kappa \sim 10^2 - 10^3 \text{ k}_\text{B} \text{T}/\mu\text{m}^2$ , corresponding to interaction energies of order  $10^2 - 10^4 \text{ k}_\text{B} \text{T}$  between micron-sized particles.

Physical settings of microscopic bodies whose interactions are of order  $\sim 10^3 \text{ k}_\text{B} \text{T}$  are characteristic to various soft matter systems, in particular colloids [37]. For example, spring constants of about  $\sim 10^2 - 10^3 \text{ k}_\text{B} \text{T}/\mu\text{m}^2$  were measured in colloidal gels [38], small lattices [39] and 2D colloidal crystals [40]. Note that elasticity can be replaced by any other conservative central force, such as magnetic [41] and electrostatic [42] interactions—all retain the Hermiticity and parity symmetries of elasticity and enter the equations of motion as an effective spring constant. Moreover, with patchy colloidal particles, one can achieve various crystal symmetries [43], such as a kagome lattice made of triblock Janus spheres [44], where the measured spring constants were  $\sim 500 \text{ k}_\text{B} \text{T}/\mu\text{m}^2$  [45]. Other relevant systems include lattices of DNA-coated colloids [46, 47] whose stiffness can be tuned by varying the length and density of the adsorbed DNA strands, colloidal lattices embedded in gels, and self-assembling microfluidic crystals [48, 49].

To observe the exceptional topology, such soft matter crystals should be subjected to viscous flow, for example in a quasi-2D microfluidic channel. The lattices can be driven by the surrounding flow, slowed down by friction [30] or held in place by boundary conditions or external forces, for example, by dynamic holographic optical tweezers [50]. What matters is the velocity of the lattice relative to the embedding fluid, which induces the hydrodynamic interactions. The geometry of the lattice can be easily adapted. In our model system (Fig. 1A), we assumed for simplicity that the particles are joined by thin struts. However, the struts can be replaced by other particles, forming for example kagome, honeycomb or square-kagome lattices. This merely implies a non-primitive unit cell with more than one particle, which would augment the non-Hermitian spectrum with additional “optical” branches. Moreover, long-range magnetic or electrostatic interactions obviate the need for direct mechanical connection among the particles. So one can leave out the struts and form, for instance, large 2D lattices of magnetic colloids [51], disks [52], hydrogel particles [53], or droplets [54], with harmonic springs induced by magnetic dipole-dipole interactions [41]. The steady state configuration of such a lattice is governed by the confining boundaries, which can be crafted to allow the passage of viscous flow. We note that the present tentative discussion is based on scaling arguments aimed to draw the relevant physical bounds on experimental feasibility, whereas the design of concrete setups would require more detailed calculation and careful calibration.

**Outlook and summary.** The discussion above on reducing to practice the proposed non-Hermitian model system understandably focused on soft materials made of micron-sized particles, a well-studied regime that

is amenable to convenient video-microscopy techniques. Can this be extended to the sub-micron regime?—Shrinking the dimensions of the system (Fig. 6) makes it generally faster (easily fulfilling condition IV) and even more overdamped, in the ultra-low Reynolds regime,  $\text{Re} \leq 10^{-6}$  (condition II). However, the thermal stability lower bound on  $\kappa$  (condition III) becomes tighter and approaches the optimal value set by condition I, at a particle size of about  $\ell \sim 100 \text{ nm}$  (keeping the same value of  $\eta u$ ). Thus, the sub-micron regime appears more challenging, though the bounds may be somewhat relaxed by increasing  $\eta u$  (shifting up the dashed line), for example using higher pressures in hardened microfluidic chambers [29, 55]. Tentative candidate systems in this regime include lattices made of DNA [47, 56], protein [57–59] and patchy nano-particles [43, 60–62]. At the other extreme, the system can be expanded up to the sub-millimetric regime, as long as the effective springs remain soft. Minding the omnipresence of both periodic lattices [63, 64] and low-Reynolds flows [65–67] in biology and biotechnology, one may speculate that non-Hermitian topological phenomena are also widespread in these realms.

To sum, the reported skewed topology with bulk Fermi arcs ending at isolated exceptional points was recently observed in a photonic crystal with radiation loss [7]. Here, we proposed a blueprint for a controllable realization of this exotic topology in ordinary elastic matter, where the analogue of radiation loss is viscoelastic dissipation. The performed analyses showed the ubiquity of exceptional points and bulk Fermi arcs in generic elastic lattices driven by viscous flow. This suggests that non-Hermitian topology—which is robust against defects and noise—can be used to develop devices in the low-Reynolds regime. For example, around the exceptional points, the system is highly responsive to variations in the control parameters, such as driving velocity or wavelength. This anomalous behavior of can be harnessed to develop new functionalities, such as ultra-sensitive detectors [19, 20]. While such future directions are intriguing, our main objective here was to propose simple viscoelastic systems, such as the one demonstrated, as an easily-accessible playground to investigate fundamental features of topological matter in the overdamped low-Reynolds regime, typical to soft and living matter.

## Appendix A: Derivation of the model

### 1. Dynamics of hydroelastic lattices

The following is a brief description of the derivation. An elastic lattice is moving in the  $x$ - $y$  plane of a thin 2D fluid layer at a velocity  $u$  relative to the fluid. In this quasi-2D geometry, the narrow dimension is  $z$  (perpendicular to the page in Fig. 1). The lattice is made of particles of size  $\ell$  joined by thin elastic rods of average length  $a$  and spring constant  $\kappa$ . The viscous drag on each particle is  $\gamma u$ , where  $\gamma$  is the friction coefficient (inverse

of the mobility). Therefore, this non-equilibrium steady-state of uniformly moving lattice requires driving forces  $\mathbf{F}$  (force per particle) that inject momentum and energy to compensate for the dissipative friction forces.

The particles' motion with respect to the fluid induces dipolar perturbations with a velocity field decaying as the inverse square of the distance,  $\sim u(\ell/r)^2$ , and this dipolar flow fields give rise to collective hydrodynamic interactions [27–30]. The hydrodynamic force  $\mathbf{f}_{ij}^{\text{hyd}}$  exerted by the  $j^{\text{th}}$  particle on the  $i^{\text{th}}$  particle is (in  $x, y$  components),

$$\begin{aligned}\mathbf{f}_{ij,x}^{\text{hyd}} &= \gamma\Lambda \sum_{j \neq i} \frac{(X_{ij}^2 - Y_{ij}^2)}{(X_{ij}^2 + Y_{ij}^2)^2} = \gamma\Lambda \sum_{j \neq i} \frac{\cos 2\theta_{ij}}{R_{ij}^2}, \quad (\text{A1}) \\ \mathbf{f}_{ij,y}^{\text{hyd}} &= \gamma\Lambda \sum_{j \neq i} \frac{2X_{ij}Y_{ij}}{(X_{ij}^2 + Y_{ij}^2)^2} = \gamma\Lambda \sum_{j \neq i} \frac{\sin 2\theta_{ij}}{R_{ij}^2},\end{aligned}$$

where the positions of the dipoles are  $\mathbf{R}_i = (X_i, Y_i)$ , and  $\mathbf{R}_{ij} = \mathbf{R}_i - \mathbf{R}_j = (X_{ij}, Y_{ij})$  are the distance vectors. In polar coordinates,  $\mathbf{R}_{ij} = (R_{ij}, \theta_{ij})$ , where  $R_{ij} = |\mathbf{R}_{ij}|$  and  $\theta_{ij}$  the angle. Equation (1) is a compact form of (A1).

The coupling constant  $\Lambda$  scales as the strength of the dipoles,  $\Lambda \sim u\ell^2$ , where  $\ell$  is the size of the particle, and  $u$  its velocity *relative to the fluid*. This defines the typical timescale  $\tau_{\text{hyd}}$  of the hydrodynamic interaction,

$$\tau_{\text{hyd}} \equiv \frac{a^3}{\Lambda} = \frac{a^3}{u\ell^2}, \quad (\text{A2})$$

the time it takes a perturbation to traverse a distance  $a$  at a sound velocity  $c_s \sim \Lambda/a^2$  (in the continuum long wavelength limit). The timescale  $\tau_{\text{hyd}}$  depends on the physical forces driving the hydrodynamic interaction. For example, in a lattice of particles sedimenting in a quasi-2D fluid, the relative velocity scales as  $u \sim \Delta\rho g\ell^2/\eta$ , where  $\Delta\rho$  is the density difference and  $\eta$  the fluid's viscosity. In the quasi-2D flow of squeezed droplets, the coupling is  $\Lambda = \ell^2 Ku$ , where  $K = u_{\text{particle}}/u_{\text{fluid}} \leq 1$  is the ratio of the velocities of particle and the surrounding fluid that drags it in the channel [27, 30].

The elastic Hookean forces are described by harmonic springs with constant  $k$  and equilibrium length  $\bar{R}_{ij}$ , the lattice constant  $a$ . The elastic forces are proportional to the change of the length,  $\Delta R_{ij} = R_{ij} - \bar{R}_{ij}$ ,

$$\mathbf{f}_i^{\text{elas}} = \kappa \Delta R_{ij} \mathbf{n}_{ij}, \quad (\text{A3})$$

where  $\mathbf{n}_{ij}$  is a unit vector in the direction of the distance  $\mathbf{R}_{ij}$ . Equation (2) is (A3) expressed in polar coordinates. In the overdamped regime, the elastic relaxation time is

$$\tau_{\text{elas}} = \frac{\gamma}{k}. \quad (\text{A4})$$

This is the typical decay time of vibrational modes in the absence of hydrodynamic driving force.

The hydroelastic number  $\epsilon$  measures the relative significance of elastic and hydrodynamic interactions (3),

$$\epsilon \equiv \frac{1/\tau_{\text{elas}}}{1/\tau_{\text{hyd}}} = \frac{\kappa a^3}{\gamma u \ell^2}.$$

Unlike odd viscosity [68] or odd elasticity [21], both hydrodynamic and elastic forces are non-circular,  $\nabla_{\mathbf{R}_{ij}} \times \mathbf{f}_{ij} = 0$ , as they conserve angular momentum.

## 2. Linear Expansion

In the overdamped low-Reynolds regime, the equations of motion are (4). At steady-state, the lattice interactions vanish by symmetry,  $\sum_{j \neq i} (\mathbf{f}_{ij}^{\text{hyd}} + \mathbf{f}_{ij}^{\text{elas}}) = 0$ , and the lattice moves uniformly at a velocity  $u = F/\gamma$ . Expansion of the equations of motion (4) in small deviations of the lattice positions around the steady-state positions,  $\mathbf{r}_j = \mathbf{R}_j - \bar{\mathbf{R}}_j$ , yields a linear dynamic equation,

$$\dot{\mathbf{r}} = \mathbf{H} \mathbf{r}, \quad (\text{A5})$$

where  $\mathbf{r}$  is  $2N$ -vector of the  $N$  particle deviations,  $\mathbf{r}_i$ . The tensor  $\mathbf{H} = \mathbf{H}_{\text{hyd}} + \epsilon \mathbf{H}_{\text{elas}}$ , which is analogous to a Hamiltonian, combines contributions from hydrodynamics and elasticity.  $\mathbf{H}$  is a  $2N \times 2N$ -matrix, composed of  $2 \times 2$  blocks  $\mathbf{H}^{ij}$  that account for interactions between the  $i^{\text{th}}$  and  $j^{\text{th}}$  particles,

$$\mathbf{H}^{ij} = \mathbf{H}_{\text{hyd}}^{ij} + \epsilon \mathbf{H}_{\text{elas}}^{ij}, \quad (\text{A6})$$

where the hydrodynamic term is

$$\mathbf{H}_{\text{hyd}}^{ij} = 2 \left( \frac{a}{\bar{R}_{ij}} \right)^3 \begin{bmatrix} \cos 3\theta_{ij} & \sin 3\theta_{ij} \\ \sin 3\theta_{ij} & -\cos 3\theta_{ij} \end{bmatrix}, \quad (\text{A7})$$

and the elastic one

$$\mathbf{H}_{\text{elas}}^{ij} = \frac{1}{2} \begin{bmatrix} 1 + \cos 2\theta_{ij} & \sin 2\theta_{ij} \\ \sin 2\theta_{ij} & 1 - \cos 2\theta_{ij} \end{bmatrix}, \quad (\text{A8})$$

which are conveniently expressed in terms of Pauli's matrices  $\boldsymbol{\sigma}_x, \boldsymbol{\sigma}_y, \boldsymbol{\sigma}_z$  (and  $\mathbf{1}$  the unity matrix),

$$\mathbf{H}_{\text{hyd}}^{ij} = 2 (a/\bar{R}_{ij})^3 (\sin 3\theta_{ij} \boldsymbol{\sigma}_x + \cos 3\theta_{ij} \boldsymbol{\sigma}_z), \quad (\text{A9})$$

$$\mathbf{H}_{\text{elas}}^{ij} = \frac{1}{2} (\mathbf{1} + \sin 2\theta_{ij} \boldsymbol{\sigma}_x + \cos 2\theta_{ij} \boldsymbol{\sigma}_z).$$

The diagonal terms ensure zero sums,  $\mathbf{H}^{ii} = -\sum_{j \neq i} \mathbf{H}^{ij}$ . Since the angles obey  $\theta_{ji} = \pi + \theta_{ij}$ , it follows from (A9) that  $\mathbf{H}_{\text{hyd}}^{ij}$  is odd with respect to particle exchange ( $i \leftrightarrow j$ ), while  $\mathbf{H}_{\text{elas}}^{ij}$  is even,

$$\mathbf{H}_{\text{hyd}}^{ji} = -\mathbf{H}_{\text{hyd}}^{ij}, \quad \mathbf{H}_{\text{elas}}^{ji} = +\mathbf{H}_{\text{elas}}^{ij}.$$

The mutual forces between the  $i^{\text{th}}$  and the  $j^{\text{th}}$  particles are  $\mathbf{f}_{ij} = \mathbf{H}^{ij}(\mathbf{r}_j - \mathbf{r}_i)$  and  $\mathbf{f}_{ji} = \mathbf{H}^{ji}(\mathbf{r}_i - \mathbf{r}_j)$ . Thus, we verify that the hydrodynamic forces violate Newton's

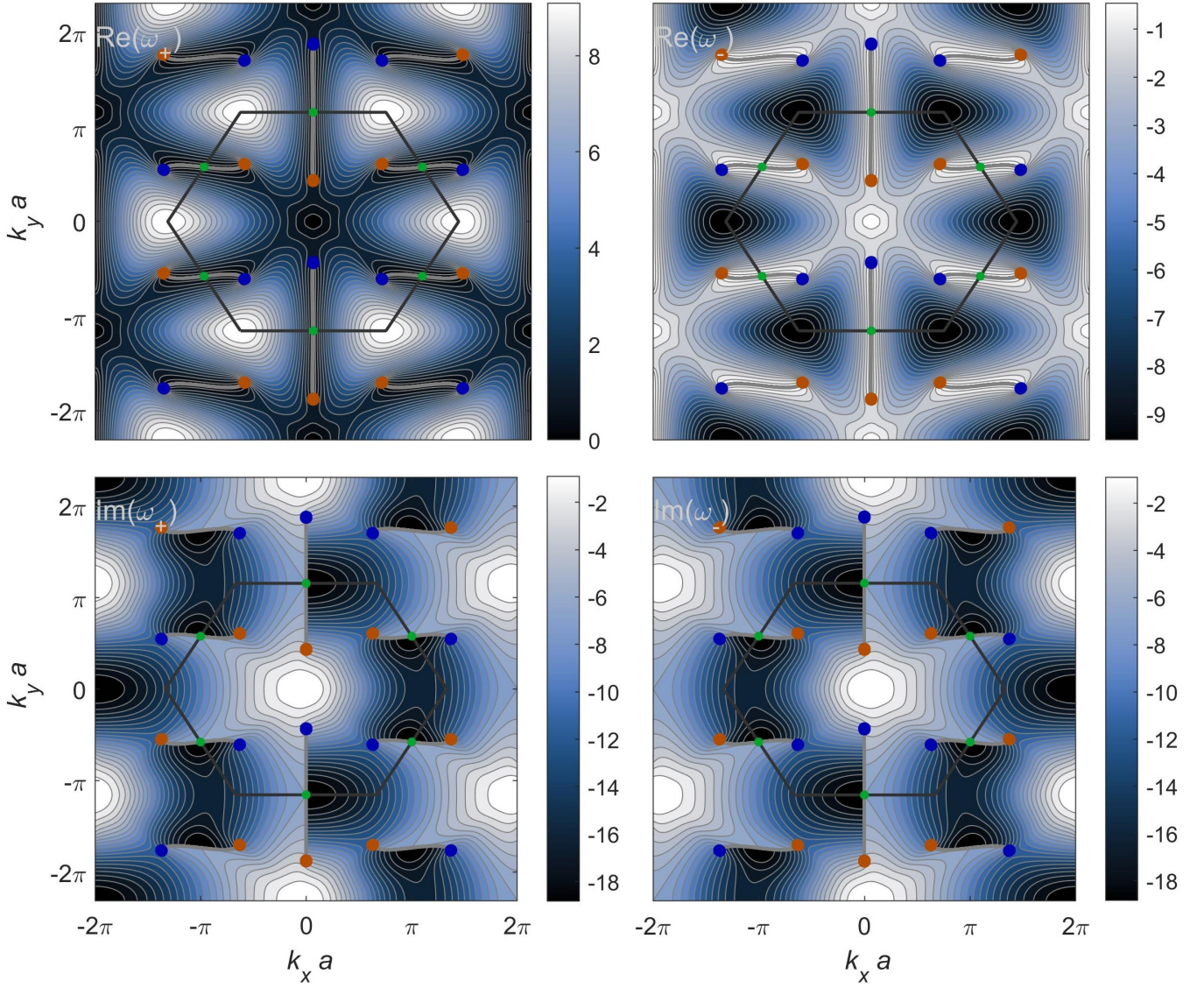


FIG. 7. **The spectrum of the triangular lattice.** The real (top) and imaginary (bottom) components of the eigenfrequencies  $\omega_+$  (left) and  $\omega_-$  (right) of a triangular lattice at  $\epsilon = \pi$  (Fig. 2B). The black hexagon is the boundary of the Brillouin zone. Shown are the Dirac points (green) at the midpoints of the Brillouin zone edges, and the ExPs with their  $+\frac{1}{2}$  (red) and  $-\frac{1}{2}$  (blue) charges. Fermi arcs are grey curves.

third law of momentum conservation, whereas the lastic forces obey it (see Fig. 1B),

$$\mathbf{f}_{ji}^{\text{hyd}} = +\mathbf{f}_{ij}^{\text{hyd}} , \quad \mathbf{f}_{ji}^{\text{elas}} = -\mathbf{f}_{ij}^{\text{elas}} .$$

While the microscopic molecular forces in the fluid obey Newton's law, the hydrodynamic interactions are *effective macroscopic* forces that do not conserve momentum. The momentum is leaking through the walls and is compensated by the driving force (*e.g.*, gravitation or pressure gradient).

### 3. Momentum space

To exploit the crystal symmetry, one represents the dynamics in the momentum space of the wave-vectors  $\mathbf{k} = (k_x, k_y)$  by Fourier transform. The linearized dynamical equations (A5,A9) are expanded in plane waves, such that the deviation of each particle from its mechanical equilibrium position  $\bar{\mathbf{R}}_j$  is

$$\mathbf{r}_j(t) = |\mathbf{k}(t)\rangle e^{i\mathbf{k}\cdot\bar{\mathbf{R}}_j} = |\mathbf{k}\rangle e^{i(\mathbf{k}\cdot\bar{\mathbf{R}}_j - \omega t)} , \quad (\text{A10})$$

where  $|\mathbf{k}(t)\rangle = |\mathbf{k}\rangle \exp(-i\omega t)$  is a 2D polarization vector in  $\mathbf{k}$ -space.

The equation of motion of  $|\mathbf{k}(t)\rangle$  is a non-unitary

Schrödinger-like equation,

$$i \frac{\partial}{\partial t} |\mathbf{k}(t)\rangle = \mathcal{H} |\mathbf{k}(t)\rangle , \quad (\text{A11})$$

whose eigenvector is  $|\mathbf{k}\rangle$  with eigenfrequency  $\omega$  (5),

$$\mathcal{H} |\mathbf{k}\rangle = \omega |\mathbf{k}\rangle .$$

The “Hamiltonian”  $\mathcal{H}$  is a  $2 \times 2$ -matrix expressed in terms of Pauli’s matrices as

$$\begin{aligned} \mathcal{H} &= \mathcal{H}_{\text{hyd}} + \epsilon \mathcal{H}_{\text{elas}} \\ &= (\Omega_x \boldsymbol{\sigma}_z + \Omega_y \boldsymbol{\sigma}_x) - \epsilon i (\omega_1 \mathbf{1} + \omega_x \boldsymbol{\sigma}_z + \omega_y \boldsymbol{\sigma}_x) . \end{aligned} \quad (\text{A12})$$

The contributions of the long-range hydrodynamic to  $\mathcal{H}$  (A12) are Fourier sums,

$$\begin{aligned} \Omega_x &= -2i \sum_{j \neq 0} \left( \frac{a}{\bar{R}_j} \right)^3 \cos 3\theta_j e^{i\mathbf{k} \cdot \bar{\mathbf{R}}_j} , \\ \Omega_y &= -2i \sum_{j \neq 0} \left( \frac{a}{\bar{R}_j} \right)^3 \sin 3\theta_j e^{i\mathbf{k} \cdot \bar{\mathbf{R}}_j} , \end{aligned}$$

where  $\bar{\mathbf{R}}_j = \bar{R}_j(\cos \theta_j, \sin \theta_j)$  are the distances of the steady-state lattice positions from an arbitrary origin particle 0. Owing to the crystal’s parity symmetry, we can rearrange the summation to be over pairs at inverse positions,  $\pm \bar{\mathbf{R}}_j$ , demonstrating that  $\Omega_x$  and  $\Omega_y$  are always real in a crystal,

$$\begin{bmatrix} \Omega_x \\ \Omega_y \end{bmatrix} = 2 \sum_{j \neq 0} \left( \frac{a}{\bar{R}_j} \right)^3 \begin{bmatrix} \cos 3\theta_j \\ \sin 3\theta_j \end{bmatrix} \sin (\mathbf{k} \cdot \bar{\mathbf{R}}_j) . \quad (\text{A13})$$

The elastic contributions in (A12) are sums over the neighbors connected by springs to particle 0,

$$\begin{aligned} \omega_x &= \frac{1}{2} \sum_{j \neq 0} \cos 2\theta_j \left( 1 - e^{i\mathbf{k} \cdot \bar{\mathbf{R}}_j} \right) , \\ \omega_y &= \frac{1}{2} \sum_{j \neq 0} \sin 2\theta_j \left( 1 - e^{i\mathbf{k} \cdot \bar{\mathbf{R}}_j} \right) , \\ \omega_1 &= \frac{1}{2} \sum_{j \neq 0} \left( 1 - e^{i\mathbf{k} \cdot \bar{\mathbf{R}}_j} \right) . \end{aligned}$$

Again, owing to the crystal parity symmetry, the sums can be rearranged, demonstrating that  $\omega_x$ ,  $\omega_y$  and  $\omega_1$  are all real,

$$\begin{bmatrix} \omega_1 \\ \omega_x \\ \omega_y \end{bmatrix} = \sum_{j \neq 0} \begin{bmatrix} 1 \\ \cos 2\theta_j \\ \sin 2\theta_j \end{bmatrix} \sin^2 \left( \frac{1}{2} \mathbf{k} \cdot \bar{\mathbf{R}}_j \right) . \quad (\text{A14})$$

The hydrodynamic and elastic interaction in a triangular lattice are shown in Fig. 8.

#### 4. Spectra

The eigenfrequencies  $\omega$  are found by solving the secular equation corresponding to (A11,A12). There are two eigenfrequency bands,

$$\begin{aligned} \omega_{\pm} &= -i\epsilon\omega_1 \pm \sqrt{(\Omega_x - i\epsilon\omega_x)^2 + (\Omega_y - i\epsilon\omega_y)^2} \\ &= -i\epsilon\omega_1 \pm \sqrt{\nu_+ \nu_-} , \end{aligned} \quad (\text{A15})$$

where  $\nu_{\pm}$  are defined as

$$\nu_{\pm} \equiv (\Omega_x - i\epsilon\omega_x) \pm i(\Omega_y - i\epsilon\omega_y) .$$

In the hydrodynamics-dominated regime,  $\epsilon \ll 1$ , the spectrum (A15) is purely real,

$$\omega_{\pm}^{\text{hyd}} \simeq \pm (\Omega_y^2 + \Omega_x^2)^{1/2} , \quad (\text{A16})$$

while in elasticity-dominated regime  $\epsilon \gg 1$  the spectrum is purely imaginary,

$$\omega_{\pm}^{\text{elas}} \simeq -i\epsilon \left[ \omega_1 \pm (\omega_x^2 + \omega_y^2)^{1/2} \right] . \quad (\text{A17})$$

The polarization eigenvectors,  $|\mathbf{k}_+\rangle$  and  $|\mathbf{k}_-\rangle$ , are

$$\begin{aligned} |\mathbf{k}_{\pm}\rangle &= \begin{bmatrix} \Omega_x - i\epsilon\omega_x + \omega_{\pm} + i\epsilon\omega_1 \\ \Omega_y - i\epsilon\omega_y \end{bmatrix} \\ &= \begin{bmatrix} \Omega_x - i\epsilon\omega_x \pm \sqrt{\nu_+ \nu_-} \\ \Omega_y - i\epsilon\omega_y \end{bmatrix} , \end{aligned} \quad (\text{A18})$$

where the eigenvalues  $\omega_{\pm}$  are given in (A15). When normalized, the eigenvectors become

$$|\mathbf{k}_{\pm}\rangle = \frac{1}{\sqrt{2} \sqrt{|\nu_+| + |\nu_-|}} \left[ i \frac{\sqrt{\nu_+} \pm \sqrt{\nu_-}}{(\sqrt{\nu_+} \mp \sqrt{\nu_-})} \right] . \quad (\text{A19})$$

#### 5. Circular polarization basis

One can represent the Hamiltonian in the basis of left and right circularly polarized unit vectors (which are the coalescing eigenstates at the ExPs),

$$\frac{1}{\sqrt{2}} \begin{bmatrix} 1 \\ \pm i \end{bmatrix} .$$

In this basis, the Hamiltonian (A12) becomes equation (6),

$$\begin{aligned} \mathcal{H} &= \mathcal{H}_{\text{hyd}} + \epsilon \mathcal{H}_{\text{elas}} \\ &= (\Omega_x \boldsymbol{\sigma}_z + \Omega_y \boldsymbol{\sigma}_x) - \epsilon i (\omega_1 \mathbf{1} + \omega_x \boldsymbol{\sigma}_x + \omega_y \boldsymbol{\sigma}_y) . \end{aligned}$$

The eigenvectors in this representation take the simple form

$$|\mathbf{k}_+\rangle = \frac{1}{\sqrt{|\nu_+| + |\nu_-|}} \begin{bmatrix} \sqrt{\nu_+} \\ \sqrt{\nu_-} \end{bmatrix} , \quad (\text{A20})$$

$$|\mathbf{k}_-\rangle = \frac{1}{\sqrt{|\nu_+| + |\nu_-|}} \begin{bmatrix} \sqrt{\nu_-} \\ \sqrt{\nu_+} \end{bmatrix} .$$

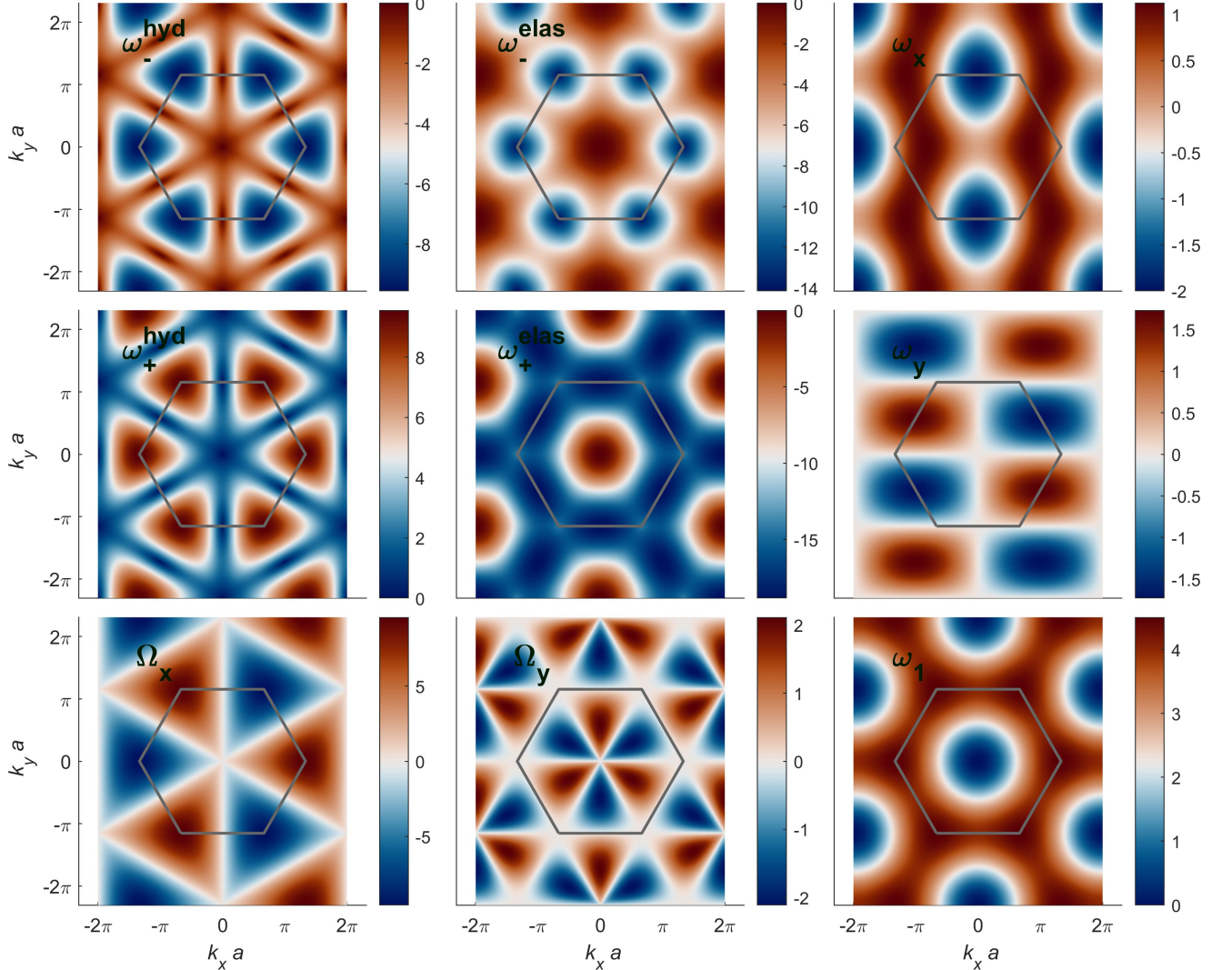


FIG. 8. **Hydrodynamic and elastic interactions and frequency bands.** The black hexagon is the boundary of the Brillouin zone. The eigenfrequencies of the purely hydrodynamic systems with negligible elasticity,  $\omega_{\pm}^{\text{hyd}}$  (A16), are real because the effective Hamiltonian is Hermitian,  $\mathcal{H} = \mathcal{H}_{\text{hyd}}$ . (top-right and center-right). In the absence of flow, the elastic system is purely damping.  $\mathcal{H} = \mathcal{H}_{\text{elas}}$  is skew-Hermitian, and therefore its spectrum,  $\omega_{\pm}^{\text{elas}}$  (A17) is purely imaginary (top-center and center). The elastic interactions,  $\Omega_x$  and  $\Omega_y$  vanish at the Dirac points, the middles of Brillouin zone edges (bottom left and center), while the elastic interactions,  $\omega_x$ ,  $\omega_y$  and  $\omega_1$ , exhibit extrema (left column).

## 6. Dirac points and cones

Dirac points occur in the purely hydrodynamic system ( $\epsilon = 0$ ), at wavevectors  $\mathbf{k}_D$  for which the hydrodynamic interaction vanishes,

$$\Omega_x = \Omega_y = 0 .$$

From (A13), one sees that this happens when  $\sin(\mathbf{k} \cdot \bar{\mathbf{R}}_j) = 0$ , that is for wavevectors that are halves of the reciprocal lattice base vectors,  $\frac{1}{2}\mathbf{b}_1, \frac{1}{2}\mathbf{b}_2$ , and their combinations,  $\mathbf{k}_D = \frac{1}{2}\beta_1\mathbf{b}_1 + \frac{1}{2}\beta_2\mathbf{b}_2$  (where  $\beta_1, \beta_2 \in \{-1, 0, 1\}$ ). In the triangular lattice, the six Dirac points are  $(\beta_1, \beta_2) = (0, \pm 1), (\pm 1, 0), (\pm 1, \pm 1)$ . Note that these

are the midpoints of the Brillouin zone edges and not the corners as in graphene.

The expansion of (A13) around the Dirac point is linear in  $\mathbf{dk} = \mathbf{k} - \mathbf{k}_D$ ,

$$\Omega_x \sim \nabla_{\mathbf{k}} \Omega_x \cdot \mathbf{dk}, \quad \Omega_y \sim \nabla_{\mathbf{k}} \Omega_y \cdot \mathbf{dk},$$

where the gradients are

$$\nabla_{\mathbf{k}} \Omega_x = 2a \sum_{j \neq 0} (-1)^{\beta_1 \alpha_1^j + \beta_2 \alpha_2^j} \begin{bmatrix} \cos \theta_j \\ \sin \theta_j \end{bmatrix} \frac{\cos 3\theta_j}{(\bar{R}_j/a)^2}, \quad (\text{A21})$$

$$\nabla_{\mathbf{k}} \Omega_y = 2a \sum_{j \neq 0} (-1)^{\beta_1 \alpha_1^j + \beta_2 \alpha_2^j} \begin{bmatrix} \cos \theta_j \\ \sin \theta_j \end{bmatrix} \frac{\sin 3\theta_j}{(\bar{R}_j/a)^2} .$$

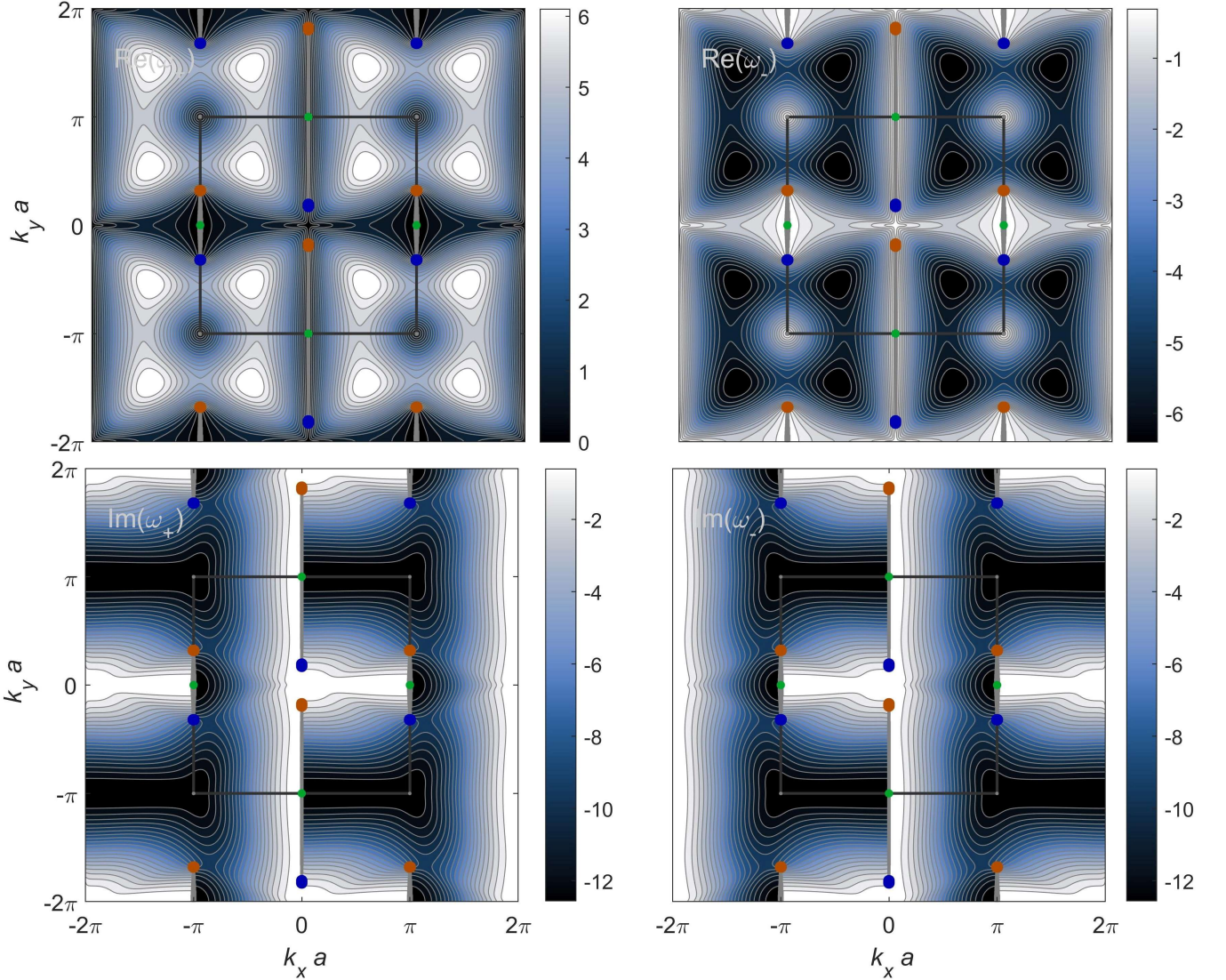


FIG. 9. **The spectrum of a square lattice.** The real (top) and imaginary (bottom) components of the eigenfrequencies,  $\omega_+$  (left) and  $\omega_-$  (right), of a square lattice at  $\epsilon = \pi$ . The black square is the boundary of the Brillouin zone. Shown are the Dirac points (green) and the ExPs with their  $+\frac{1}{2}$  (red) and  $-\frac{1}{2}$  (blue) charges. Bulk Fermi arcs are grey curves.

The  $\alpha_1^j$  and  $\alpha_2^j$  in (A21) are the indices of the lattice points,  $\bar{\mathbf{R}}_j = \alpha_1^j \mathbf{a}_1 + \alpha_2^j \mathbf{a}_2$ , with the basis vectors,  $\mathbf{a}_1$  and  $\mathbf{a}_2$ . It is straightforward to verify that the gradients at the Dirac point are orthogonal,

$$\nabla_{\mathbf{k}} \Omega_x \cdot \nabla_{\mathbf{k}} \Omega_y = 0, \quad (\text{A22})$$

resulting in an elliptic cone (Fig. 2A). It is also useful to note that, at the Dirac points, the elastic interactions,  $\omega_x$ ,  $\omega_y$  and  $\omega_1$ , have extrema (minima, maxima, and saddles), and are therefore constant to first order in  $d\mathbf{k}$  (Fig. 8).

## 7. Exceptional points and Fermi arcs

Exceptional points (ExPs) occur when both eigenfrequencies (A15) and eigenvectors (A19) coincide,

$$\omega_+ = \omega_- = -i\epsilon\omega_1, \quad (\text{A23})$$

$$|\mathbf{k}_+\rangle = |\mathbf{k}_-\rangle = \frac{1}{\sqrt{2}} \begin{bmatrix} 1 \\ \pm i \end{bmatrix},$$

where the  $\pm$  signs correspond to the paired ExPs. In the circular polarization basis, the eigenvectors at the ExPs are the unit vectors,

$$|\mathbf{k}_+\rangle = \begin{bmatrix} 1 \\ 0 \end{bmatrix}, \quad |\mathbf{k}_-\rangle = \begin{bmatrix} 0 \\ 1 \end{bmatrix}.$$

ExPs are positioned exactly where the determinant,  $\nu_+ \nu_-$ , in (A15) vanishes. In other words, when  $\nu_+ = 0$

or  $\nu_- = 0$ , which amounts to the double condition (9),

$$\frac{\Omega_y}{\omega_x} = -\frac{\Omega_x}{\omega_y} = \pm\epsilon.$$

As one varies  $\epsilon$ , the ExPs move along the 1D curve

$$\Omega_x\omega_x + \Omega_y\omega_y = 0, \quad (\text{A24})$$

from the Dirac cones at  $\epsilon = 0$  to the Brillouin zone corners (or its center) at  $\epsilon = \infty$ . The stretch of the trajectory between the two ExPs is the *Fermi arc*. Along these trajectories, the eigenfrequencies are

$$\begin{aligned} \omega_{\pm} &= -i\epsilon\omega_1 \pm [(\Omega_x^2 + \Omega_y^2) - \epsilon^2(\omega_x^2 + \omega_y^2)]^{1/2} \quad (\text{A25}) \\ &= -i\epsilon\omega_1 \pm (s^2 - \epsilon^2)^{1/2}(\omega_x^2 + \omega_y^2)^{1/2}, \end{aligned}$$

where  $s \equiv \Omega_x/\omega_y = -\Omega_x/\omega_y$  is the coordinate along the trajectory, from  $s = 0$ , the Dirac point, through  $s = \epsilon$ , the ExP, to the corner of the Brillouin zone  $s = \infty$  (the four S-shaped arcs), or its center (the two straight arcs). The exceptional point is the position of a *bifurcation* transition where the branch-cut of the square root stretches along the Fermi arc.

## 8. Bulk Fermi arcs are generic

The bulk Fermi arcs observed in the triangular (Figs. 2,7) or the square (Fig. 9) lattices are a *generic* phenomenon of the hydroelastic lattice. They emerge as soon as symmetry is broken, at  $\epsilon \neq 0$ , when the skew-Hermitian elasticity is introduced. To see this formally, one may examine the emergence of arcs for small  $\epsilon$ . Then, the exceptional point condition (9) can be linearly expanded in small deviations from the Dirac point,  $\mathbf{dk} = \mathbf{k} - \mathbf{k}_D$  (A21). The double condition (9) becomes a linear equation in  $\mathbf{dk}$ ,

$$\begin{bmatrix} \nabla_{\mathbf{k}}\Omega_x^{\text{I}} \\ \nabla_{\mathbf{k}}\Omega_y^{\text{I}} \end{bmatrix} \mathbf{dk} = \pm\epsilon \begin{bmatrix} -\omega_y \\ \omega_x \end{bmatrix}, \quad (\text{A26})$$

where the  $\pm$  signs correspond to the two ExPs. Since the gradients are linearly-independent (A22), solutions always exist, and the positions of the ExPs are

$$\mathbf{dk} = \pm\epsilon \begin{bmatrix} \nabla_{\mathbf{k}}\Omega_x \\ |\nabla_{\mathbf{k}}\Omega_x|^2 \\ \nabla_{\mathbf{k}}\Omega_y \\ |\nabla_{\mathbf{k}}\Omega_y|^2 \end{bmatrix} \begin{bmatrix} -\omega_y \\ \omega_x \end{bmatrix}. \quad (\text{A27})$$

Hence, the arcs and the ExPs are generic. The bulk Fermi arc stretches between the two solutions, and its size grows linearly with  $\epsilon$ .

## 9. Berry's phase and the topological charges

In the momentum representation, Berry's connections are the vectors [35],

$$\mathcal{A}_{\pm}(\mathbf{k}) = i \langle \mathbf{k}_{\pm} | \nabla_{\mathbf{k}} | \mathbf{k}_{\pm} \rangle, \quad (\text{A28})$$

corresponding to the eigenvectors  $|\mathbf{k}_{\pm}\rangle$ . For convenience, we write the normalized eigenvectors as Jones polarization vectors,

$$|\mathbf{k}_{+}\rangle = \begin{bmatrix} \sqrt{c} e^{i\alpha_{+}} \\ \sqrt{1-c} e^{i\alpha_{-}} \end{bmatrix}, \quad |\mathbf{k}_{-}\rangle = \begin{bmatrix} \sqrt{1-c} e^{i\alpha_{-}} \\ \sqrt{c} e^{i\alpha_{+}} \end{bmatrix}. \quad (\text{A29})$$

In this notation, we find that the Berry connections are simply

$$\mathcal{A}_{\pm}(\mathbf{k}) = -c\nabla_{\mathbf{k}}\alpha_{+} - (1-c)\nabla_{\mathbf{k}}\alpha_{-}. \quad (\text{A30})$$

For the eigenvectors (A18), the Jones parameters are

$$\begin{aligned} c &= \frac{|\sqrt{\nu_{+}} + \sqrt{\nu_{-}}|^2}{2(|\nu_{+}| + |\nu_{-}|)}, \\ \alpha_{+} &= \arg(\sqrt{\nu_{+}} + \sqrt{\nu_{-}}), \\ \alpha_{-} &= \arg(\sqrt{\nu_{+}} - \sqrt{\nu_{-}}). \end{aligned}$$

The Berry phases  $\gamma_{\pm}$  are the path integrals

$$\gamma_{\pm} = \oint \mathcal{A}_{\pm}(\mathbf{k}) \cdot d\mathbf{k}. \quad (\text{A31})$$

To find the Berry phase of the ExPs, we integrate over a small circular counterclockwise path around each point. For example, consider the point where  $\nu_{+} = 0$ . In the vicinity of an ExP,  $c \simeq \frac{1}{2}$ , and the connections are therefore,

$$\mathcal{A}_{\pm}(\mathbf{k}) \simeq -\frac{1}{2}\nabla_{\mathbf{k}}\alpha_{+} - \frac{1}{2}\nabla_{\mathbf{k}}\alpha_{-} \simeq -\frac{1}{2}\nabla_{\mathbf{k}}\arg\nu_{+}. \quad (\text{A32})$$

Along the circular integration path, the phase  $\arg\nu_{+}$  passes all quadrants. In particular, it passes through the branch cut,  $\arg\nu_{+} = \pm\pi$ , where it jumps by  $\pm 2\pi$ , depending on the gradients of  $\nu_{+}$ . Thus, we find that Berry's phase is  $\gamma_{\pm} = \pm\pi$ . Likewise, at the other ExP, Berry's phase takes the opposite sign,  $\gamma_{\pm} = \mp\pi$ . Altogether, we find that the corresponding topological charges are  $q_{\pm} = \gamma_{\pm}/(2\pi) = \pm\frac{1}{2}$ .

## 10. Vorticity and Topological Charges

Another way to find the topological charges is through the vorticity of the eigenfrequency band-gap,  $\Delta\omega = \omega_{+} - \omega_{-}$ , defined as [4]

$$\mathcal{V} = -\frac{1}{2\pi} \oint_{\Gamma} d\mathbf{k} \cdot \nabla_{\mathbf{k}} \arg(\Delta\omega), \quad (\text{A33})$$

where  $\omega_{\pm}$  are the given in (A13). Since,  $\Delta\omega = \omega_{+} - \omega_{-} = 2\sqrt{\nu_{+}\nu_{-}}$ , we find that the vorticity is

$$\mathcal{V} = -\frac{1}{4\pi} \oint_{\Gamma} d\mathbf{k} \cdot \nabla_{\mathbf{k}} (\arg\nu_{+} + \arg\nu_{-}). \quad (\text{A34})$$

As in the case of the Berry phase, the vorticity around the ExPs is determined by their branch-cuts. Namely, the jumps of  $\arg\nu_{\pm}$  by  $\pm 2\pi$  when passing through the branch cuts yield the topological charges  $q_{\pm} = \pm\frac{1}{2}$ .

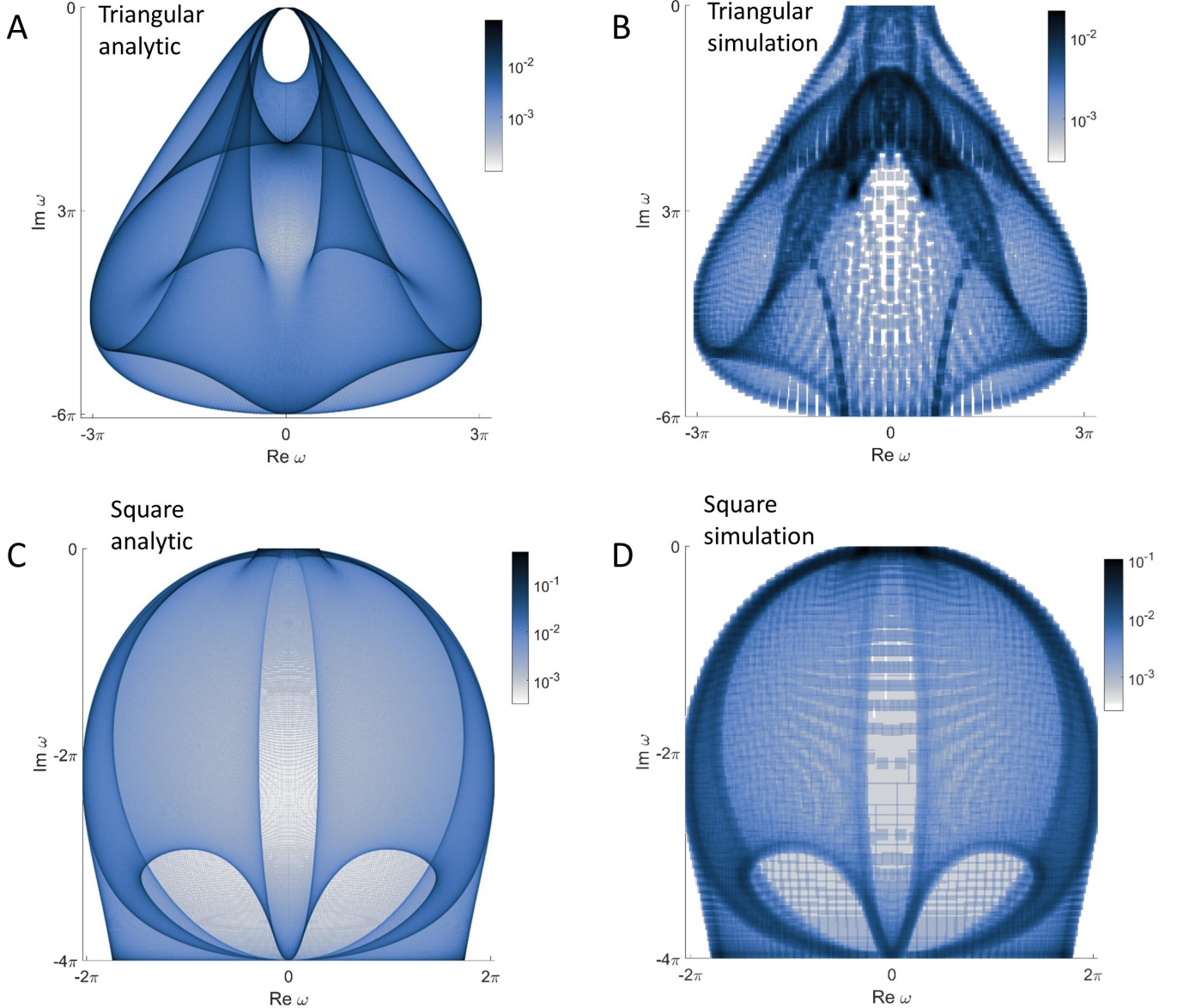


FIG. 10. **Density of states  $g(\omega)$ : analytic solution vs. simulation.** (A-B):  $g(\omega)$  for triangular lattice, analytic (A) and simulation (B), for  $\epsilon = \pi$ . The simulated system is a  $121 \times 121$  triangular lattice with periodic boundary conditions (a torus). The spectrum is obtained by Fourier analysis of the motion computed from the dynamical equation (4). The simulated  $g(\omega)$  exhibits general similarity to the analytic solution. The incommensurability of the four-fold symmetry of the torus and the six-fold symmetry of the lattice results (C-D):  $g(\omega)$  for square lattice, analytic (A) and simulation of a  $121 \times 121$  lattice (B), for  $\epsilon = \pi$ . The correspondence between the simulation and the analytic solution is excellent, owing to the commensurable four-fold symmetry of the lattice and the periodic boundary conditions, with some coarseness due to the finite size of the simulated system.

---

[1] C. M. Bender and S. Boettcher, Real spectra in non-hermitian hamiltonians having pt symmetry, *Phys. Rev. Lett.* **80**, 5243 (1998).

[2] J. Doppler, A. A. Mailybaev, J. Bhm, U. Kuhl, A. Girschik, F. Libisch, T. J. Milburn, P. Rabl, N. Moiseyev, and S. Rotter, Dynamically encircling an exceptional point for asymmetric mode switching, *Nature* **537**, 76 (2016).

[3] R. El-Ganainy, K. G. Makris, M. Khajavikhan, Z. H. Musslimani, S. Rotter, and D. N. Christodoulides, Non-hermitian physics and pt symmetry, *Nat. Phys.* **14**, 11 (2018).

[4] H. Shen, B. Zhen, and L. Fu, Topological band theory for non-hermitian hamiltonians, *Phys. Rev. Lett.* **120**, 146402 (2018).

[5] N. Moiseyev, *Non-Hermitian quantum mechanics* (Cambridge University Press, Cambridge ; New York, 2011).

[6] E. J. Bergholtz, J. C. Budich, and F. K. Kunst, Exceptional topology of non-hermitian systems, *Review of Modern Physics* **93**, 015005 (2021).

[7] H. Zhou, C. Peng, Y. Yoon, C. W. Hsu, K. A. Nelson, L. Fu, J. D. Joannopoulos, M. Soljai, and B. Zhen, Observation of bulk fermi arc and polarization half charge from paired exceptional points, *Science* **359**, 1009 (2018).

[8] L. Feng, R. El-Ganainy, and L. Ge, Non-hermitian photonics based on paritytime symmetry, *Nat. Photonics* **11**, 752 (2017).

[9] M. A. Miri and A. Alu, Exceptional points in optics and photonics, *Science* **363** (2019).

[10] S. Weidemann, M. Kremer, T. Helbig, T. Hofmann, A. Stegmaier, M. Greiter, R. Thomale, and A. Szameit, Topological funneling of light, *Science* **368**, 311 (2020).

[11] E. Rivet, A. Brandstötter, K. G. Makris, H. Lissek, S. Rotter, and R. Fleury, Constant-pressure sound waves in non-hermitian disordered media, *Nat. Phys.* **14**, 942 (2018).

[12] W. Zhu, X. Fang, D. Li, Y. Sun, Y. Li, Y. Jing, and H. Chen, Simultaneous observation of a topological edge state and exceptional point in an open and non-hermitian acoustic system, *Phys. Rev. Lett.* **121**, 124501 (2018).

[13] G. Ma, M. Xiao, and C. T. Chan, Topological phases in acoustic and mechanical systems, *Nature Reviews Physics* **1**, 281 (2019).

[14] H. Xu, D. Mason, L. Jiang, and J. G. E. Harris, Topological energy transfer in an optomechanical system with exceptional points, *Nature* **537**, 80 (2016).

[15] J. Schindler, A. Li, M. C. Zheng, F. M. Ellis, and T. Kottos, Experimental study of active lrc circuits with  $\mathcal{PT}$  symmetries, *Phys. Rev. A* **84**, 040101 (2011).

[16] Z. Zhang, Y. Zhang, J. Sheng, L. Yang, M.-A. Miri, D. N. Christodoulides, B. He, Y. Zhang, and M. Xiao, Observation of parity-time symmetry in optically induced atomic lattices, *Phys. Rev. Lett.* **117**, 123601 (2016).

[17] A. Guo, G. J. Salamo, D. Duchesne, R. Morandotti, M. Volatier-Ravat, V. Aimez, G. A. Siviloglou, and D. N. Christodoulides, Observation of  $\mathcal{PT}$ -symmetry breaking in complex optical potentials, *Phys. Rev. Lett.* **103**, 093902 (2009).

[18] A. Regensburger, C. Bersch, M.-A. Miri, G. Onishchukov, D. N. Christodoulides, and U. Peschel, Parity-time synthetic photonic lattices, *Nature* **488**, 167 (2012).

[19] J. Wiersig, Enhancing the sensitivity of frequency and energy splitting detection by using exceptional points: Application to microcavity sensors for single-particle detection, *Phys. Rev. Lett.* **112**, 203901 (2014).

[20] H. Hodaei, A. U. Hassan, S. Wittek, H. Garcia-Gracia, R. El-Ganainy, D. N. Christodoulides, and M. Khajavikhan, Enhanced sensitivity at higher-order exceptional points, *Nature* **548**, 187 (2017).

[21] C. Scheibner, A. Souslov, D. Banerjee, P. Surwka, W. T. M. Irvine, and V. Vitelli, Odd elasticity, *Nat. Phys.* **16**, 475 (2020).

[22] C. Scheibner, W. T. M. Irvine, and V. Vitelli, Non-hermitian band topology and skin modes in active elastic media, *PRL* **125**, 118001 (2020).

[23] X. Wan, A. M. Turner, A. Vishwanath, and S. Y. Savrasov, Topological semimetal and fermi-arc surface states in the electronic structure of pyrochlore iridates, *Phys. Rev. B* **83**, 205101 (2011).

[24] S.-Y. Xu, C. Liu, S. K. Kushwaha, R. Sankar, J. W. Krizan, I. Belopolski, M. Neupane, G. Bian, N. Alidoust, T.-R. Chang, H.-T. Jeng, C.-Y. Huang, W.-F. Tsai, H. Lin, P. P. Shibayev, F.-C. Chou, R. J. Cava, and M. Z. Hasan, Observation of fermi arc surface states in a topological metal, *Science* **347**, 294 (2015).

[25] B. Yang, Q. Guo, B. Tremain, R. Liu, L. E. Barr, Q. Yan, W. Gao, H. Liu, Y. Xiang, J. Chen, C. Fang, A. Hibbins, L. Lu, and S. Zhang, Ideal weyl points and helicoid surface states in artificial photonic crystal structures, *Science* **359**, 1013 (2018).

[26] N. Morali, R. Batabyal, P. K. Nag, E. Liu, Q. Xu, Y. Sun, B. Yan, C. Felser, N. Avraham, and H. Beidenkopf, Fermi-arc diversity on surface terminations of the magnetic weyl semimetal  $\text{Co}_3\text{Sn}_2\text{S}_2$ , *Science* **365**, 1286 (2019).

[27] T. Beatus, T. Tlusty, and R. Bar-Ziv, Phonons in a one-dimensional microfluidic crystal, *Nat. Phys.* **2**, 743 (2006).

[28] M. Baron, J. Bawdziewicz, and E. Wajnryb, Hydrodynamic crystals: Collective dynamics of regular arrays of spherical particles in a parallel-wall channel, *Phys. Rev. Lett.* **100**, 174502 (2008).

[29] T. Beatus, R. H. Bar-Ziv, and T. Tlusty, The physics of 2d microfluidic droplet ensembles, *Phys. Rep.* **516**, 103 (2012).

[30] T. Beatus, I. Shani, R. H. Bar-Ziv, and T. Tlusty, Two-dimensional flow of driven particles: a microfluidic pathway to the non-equilibrium frontier, *Chem. Soc. Rev.* **46**, 5620 (2017).

[31] N. Liron and S. Mochon, Stokes flow for a stokeslet between two parallel flat plates, *J. Engrg. Math.* **10**, 287 (1976).

[32] B. Cui, H. Diamant, B. Lin, and S. A. Rice, Anomalous hydrodynamic interaction in a quasi-two-dimensional suspension, *Phys. Rev. Lett.* **92**, 258301 (2004).

[33] L. Landau and E. Lifshitz, On the theory of the dispersion of magnetic permeability in ferromagnetic bodies, *Phy. Z. Sowjetunion* **8**: 153 (1935).

[34] D. R. Yarkony, Diabolical conical intersections, *Rev. Mod. Phys.* **68**, 985 (1996).

[35] M. V. Berry, Quantal phase factors accompanying adiabatic changes, *Proc Roy Soc A* **392**, 45 (1984).

[36] L. Van Hove, The occurrence of singularities in the elastic frequency distribution of a crystal, *Phys. Rev.* **89**, 1189 (1953).

[37] S. Safran, *Statistical thermodynamics of surfaces, interfaces, and membranes* (CRC Press, 2018).

[38] A. D. Dinsmore, V. Prasad, I. Y. Wong, and D. A. Weitz, Microscopic structure and elasticity of weakly aggregated colloidal gels, *PRL* **96**, 185502 (2006).

[39] B. J. Park, B. Lee, and T. Yu, Pairwise interactions of colloids in two-dimensional geometric confinement, *Soft Matter* **10**, 9675 (2014).

[40] I. Buttinoni and R. P. A. Dullens, Mechanical properties of colloidal crystals at fluid interfaces, *Journal of Physics: Materials* **4**, 025001 (2021).

[41] P. Keim, G. Maret, U. Herz, and H. H. von Grünberg, Harmonic lattice behavior of two-dimensional colloidal crystals, *PRL* **92**, 215504 (2004).

[42] C. P. Kelleher, R. E. Guerra, A. D. Hollingsworth, and P. M. Chaikin, Phase behavior of charged colloids at a fluid interface, *PRE* **95**, 022602 (2017).

[43] Z. Zhang and S. C. Glotzer, Self-assembly of patchy particles, *Nano Lett.* **4**, 1407 (2004).

[44] Q. Chen, S. C. Bae, and S. Granick, Directed self-assembly of a colloidal kagome lattice, *Nature* **469**, 381 (2011).

[45] X. Mao, Q. Chen, and S. Granick, Entropy favours open colloidal lattices, *Nature Materials* **12**, 217 (2013).

[46] Y. Wang, Y. Wang, X. Zheng, . Ducrot, J. S. Yodh, M. Weck, and D. J. Pine, Crystallization of dna-coated colloids, *Nature Communications* **6**, 7253 (2015).

[47] W. B. Rogers, W. M. Shih, and V. N. Manoharan, Using dna to program the self-assembly of colloidal nanoparticles and microparticles, *Nature Reviews Materials* **1**, 16008 (2016).

[48] W. Lee, H. Amini, H. A. Stone, and D. Di Carlo, Dynamic self-assembly and control of microfluidic particle crystals, *Proc Natl Acad Sci USA* **107**, 22413 (2010).

[49] W. E. Uspal and P. S. Doyle, Self-organizing microfluidic crystals, *Soft Matter* **10**, 5177 (2014).

[50] J. E. Curtis, B. A. Koss, and D. G. Grier, Dynamic holographic optical tweezers, *Optics Communications* **207**, 169 (2002).

[51] K. Zahn and G. Maret, Dynamic criteria for melting in two dimensions, *PRL* **85**, 3656 (2000).

[52] B. A. Grzybowski, H. A. Stone, and G. M. Whitesides, Dynamics of self assembly of magnetized disks rotating at the liquidair interface, *Proceedings of the National Academy of Sciences* **99**, 4147 (2002).

[53] D. K. Hwang, D. Dendukuri, and P. S. Doyle, Microfluidic-based synthesis of non-spherical magnetic hydrogel microparticles, *Lab Chip* **8**, 1640 (2008).

[54] G. Katsikis, J. S. Cybulski, and M. Prakash, Synchronous universal droplet logic and control, *Nature Physics* **11**, 588 (2015).

[55] I. Shani, T. Beatus, R. H. Bar-Ziv, and T. Thusty, Long-range orientational order in two-dimensional microfluidic dipoles, *Nature Physics* **10**, 140 (2014).

[56] R. V. Thaner, Y. Kim, T. I. N. G. Li, R. J. Macfarlane, S. T. Nguyen, M. Olvera de la Cruz, and C. A. Mirkin, Entropy-driven crystallization behavior in dna-mediated nanoparticle assembly, *Nano Lett.* **15**, 5545 (2015).

[57] J. C. Sinclair, K. M. Davies, C. Vnien-Bryan, and M. E. M. Noble, Generation of protein lattices by fusing proteins with matching rotational symmetry, *Nature Nanotechnology* **6**, 558 (2011).

[58] A. J. Ben-Sasson, J. L. Watson, W. Sheffler, M. C. Johnson, A. Bittleston, L. Somasundaram, J. Decarreau, F. Jiao, J. Chen, I. Mela, A. A. Drabek, S. M. Jarrett, S. C. Blacklow, C. F. Kaminski, G. L. Hura, J. J. De Yoreo, J. M. Kollman, H. Ruohola-Baker, E. Derivery, and D. Baker, Design of biologically active binary protein 2d materials, *Nature* **589**, 468 (2021).

[59] S. Zhang, R. G. Alberstein, J. J. De Yoreo, and F. A. Tezcan, Assembly of a patchy protein into variable 2d lattices via tunable multiscale interactions, *Nature Communications* **11**, 3770 (2020).

[60] D. J. Lunn, J. R. Finnegan, and I. Manners, Self-assembly of patchy nanoparticles: a versatile approach to functional hierarchical materials, *Chem. Sci.* **6**, 3663 (2015).

[61] V. Liljeström, J. Seitsonen, and M. A. Kostiainen, Electrostatic self-assembly of soft matter nanoparticle cocrystals with tunable lattice parameters, *ACS Nano* **9**, 11278 (2015).

[62] Z.-W. Li, Y.-W. Sun, Y.-H. Wang, Y.-L. Zhu, Z.-Y. Lu, and Z.-Y. Sun, Kinetics-controlled design principles for two-dimensional open lattices using atom-mimicking patchy particles, *Nanoscale* **12**, 4544 (2020).

[63] P. Messner, C. Schäffer, E.-M. Egelseer, and U. B. Sleytr, Occurrence, structure, chemistry, genetics, morphogenesis, and functions of s-layers, in *Prokaryotic cell wall compounds* (Springer, 2010) pp. 53–109.

[64] M. Charrier, D. Li, V. R. Mann, L. Yun, S. Jani, B. Rad, B. E. Cohen, P. D. Ashby, K. R. Ryan, and C. M. Ajo-Franklin, Engineering the s-layer of caulobacter crescentus as a foundation for stable, high-density, 2d living materials, *ACS Synth. Biol.* **8**, 181 (2019).

[65] E. M. Purcell, Life at low reynolds number, *American Journal of Physics* **45**, 3 (1977).

[66] J. P. Brody, P. Yager, R. E. Goldstein, and R. H. Austin, Biotechnology at low reynolds numbers, *Biophysical Journal* **71**, 3430 (1996).

[67] E. Lauga and T. R. Powers, The hydrodynamics of swimming microorganisms, *Reports on Progress in Physics* **72**, 096601 (2009).

[68] J. E. Avron, Odd viscosity, *J. Stat. Phys.* **92**, 543 (1998).